Constricted migration contributes to persistent 3D genome structure changes associated with an invasive phenotype in melanoma cells

Rosela Golloshi[1,*], Rebeca San Martin[1], Priyojit Das[2], Thomas Isaac Raines[1], Delaney Thurston[1], Trevor Freeman[1], Rachel Patton McCord[1,3,*]

[1] Biochemistry & Cellular and Molecular Biology Department, University of Tennessee, Knoxville, TN

[2] UT-ORNL Graduate School of Genome Science and Technology, University of Tennessee, Knoxville, TN

[3] Lead Contact

[*] Correspondence: rgollosh@vols.utk.edu (R.G.), rmccord@utk.edu (R.P.M.)

Summary

To spread from a localized tumor, metastatic cancer cells must squeeze through constrictions that cause major nuclear deformations. Since chromosome structure affects nucleus stiffness, gene regulation and DNA repair, here we investigate how confined migration affects or is affected by 3D genome structure. Using melanoma (A375) cells, we identify phenotypic differences in cells that have undergone 10 rounds of constricted migration. These cells display a stable increase in migration efficiency, elongated morphology, and an abnormal distribution of Lamin A/C and heterochromatin. Using Hi-C, we observe changes in chromosome spatial compartmentalization specific to constricted cells and related alterations in expression of genes associated with migration and metastasis. These cells also show increased nuclear deformations when cultured in a 3D collagen matrix and altered behavior when co-cultured with fibroblasts in organoids. Our observations reveal a relationship between chromosome structure changes, metastatic gene signatures, and the abnormal nuclear appearance of aggressive melanoma.

Introduction

Despite significant improvements in the diagnosis and treatment of cancer, most patients with advanced metastatic disease face a terminal illness incurable by current therapeutic methods. The dissemination of cancer cells from the primary tumor and the formation of new tumor colonies at distant sites involves a complex multi-step invasion-metastasis cascade (Lambert et al., 2017, Gupta and Massague, 2006, Chambers et al., 2002, Fidler, 2003). To metastasize, cancer cells must squeeze through constrictions of the extracellular matrix or endothelial lining that are much smaller than their nucleus, causing major nuclear deformations. While the cell membrane and cytoplasm are quite elastic, the ability of the cell's nucleus to withstand large deformations and squeeze through these small spaces is limited by its size and stiffness, posing challenges to confined migration (Davidson et al., 2014, Fu et al., 2012, Wolf et al., 2013, Friedl et al., 2011). Nuclear stiffness and deformability depend on two major components: lamin proteins (Lamin A/C and Lamin B) and the chromatin (Stephens et al., 2017, Harada et al., 2014, Davidson et al., 2014).

Lamin A/C expression and its stoichiometric relation to Lamin B contributes to nuclear mechanical properties (Harada et al., 2014). Low expression levels of Lamin A/C lead to decreased nuclear stiffness and increased deformability (Lammerding et al., 2006). Likely resulting from increased nuclear flexibility, decreased expression of Lamin A/C has been shown to promote constricted migration in mouse embryonic fibroblasts (MEFs). Conversely, increased expression of Lamin A/C inhibits migration through constrictions in neutrophils (Davidson et al., 2014, Rowat et al., 2013). Given this relation between lamin content and confined migration, it is not surprising that low levels of Lamin A/C are correlated with the increased aggressiveness of some cancers (Broers et al., 1993, Wazir et al., 2013). However, not all invasive cancers downregulate their Lamin A/C expression; in fact, an increase in Lamin A/C is associated with progression of aggressive cancers such as colorectal and skin basal cell skin carcinoma (Willis et al., 2008, Venables et al., 2001). Decreased lamin content during confined migration can even be deleterious as it jeopardizes the integrity of the nuclear envelope and increases the probability of nuclear rupture events as the nucleus passes through a constriction. Such nuclear rupture can lead to DNA damage, DNA loss, and genomic aberrations (Denais et al., 2016, Irianto et al., 2017a).

In addition to the complex role of lamin content, recent work emphasizes the additional role of chromatin in mechano-sensing, nuclear stiffness, and invasiveness (Miroshnikova et al., 2017, Stephens et al., 2017). The two-meter chromatin fiber is packaged into the nucleus in a complex 3D architecture that informs DNA replication, repair, and gene regulation (Marchal et al., 2019, Krijger and de Laat, 2016, Spielmann et al., 2018). Regions of the genome are marked with different histone modifications and become spatially compartmentalized into heterochromatin and euchromatin through different mechanisms, such as tethering to nuclear structures like the lamina, or due to phase separation (van Steensel and Belmont, 2017, Strom et al., 2017). Genes within less-accessible heterochromatin tend to be inactive while those localized to more accessible euchromatin tend to be active or poised for quick transcriptional activation (Gaspar-Maia et al., 2011, van Steensel and Belmont, 2017). Chromatin state has also been shown to influence nuclear physical properties: increased levels of heterochromatin increase nuclear stiffness while increased euchromatin levels decrease stiffness and increase nuclear deformability (Stephens et al., 2017, Stephens et al., 2018). Such global changes in chromatin state can also influence confined migration; for example, increasing euchromatin or decreasing heterochromatin inhibits mouse melanoma cell migration (Gerlitz and Bustin, 2010). Mounting evidence also points to the effect that extracellular physical forces have on nuclear mechanics and chromosome structure. Nuclei aspirated into narrow micropipettes exhibit stretching of chromatin domains that is sometimes irreversible (Irianto et al., 2017b), and external cellular forces can affect gene expression through direct chromatin deformations (Tajik et al., 2016). Despite such connections between chromatin structure, nucleus deformation, and nucleus mechanics, it is not fully understood whether the 3D organization of the genome affects or is affected by confined migration.

Ever-improving microscopic techniques and the development of chromosome conformation capture approaches have revolutionized our understanding of 3D genome architecture in the past decade (Dekker et al., 2002, Bickmore and van Steensel, 2013, Rowley and Corces, 2018, Pombo and Dillon, 2015, Abbas et al., 2019). Chromosomes are folded at different length scales into loops, topologically associating domains (TADs), active and inactive (A/B) compartments,

and chromosomal territories. How these layers of structure are affected by physical nucleus shape changes such as the kind experienced during constricted migration remains unknown. Previous work has shown that 3D chromosome organization changes correlate with the progression of cancer (Taberlay et al., 2016, Barutcu et al., 2015, Zhou et al., 2019) and that both the formation and downstream effect of chromosomal translocations in cancer progression is influenced by 3D genome structure (Zhang et al., 2012, Hnisz et al., 2016). In addition, some changes have been noted in the 3D genome structures of neutrophils that have undergone constricted migration (Jacobson et al., 2018). Taken together, previous evidence suggests that chromosome structure may influence a cancer cell's ability to undergo confined migration, that changes in chromosome structure could be caused by nuclear deformation, and that such chromosome structure changes could influence gene regulation and cancer cell phenotype. In this study, we seek to unite these previous ideas and test this hypothesis that certain 3D genome structures of cancer cells facilitate or are changed by constricted migration.

Here, we use invasive human melanoma cells (A375) to investigate the properties of the nucleus and 3D chromosome structure that accompany confined migration. In line with previous reports using osteosarcoma cells (U2OS) (Irianto et al., 2017a), we find that A375 cells that have migrated numerous times through tight constrictions are phenotypically distinct from cells that do not pass through constrictions. We find that these cells exhibit specific and stable alterations in 3D genome organization, particularly at the level of A/B compartmentalization, lamin localization, and gene expression patterns. Our results suggest that 3D genome architecture influences the ability of cancer cells to undergo constricted migration and raises the possibility that changes take place after constricted migration which confer a higher metastatic efficiency for subsequent rounds of migration through constrictions.

Keywords

Constricted migration, Hi-C, 3D genome, melanoma, genome compartments, metastasis, heterochromatin, lamin, nucleus structure

Glossary

Control A375 cells that have not undergone constricted migration but have been grown in a 2D culture dish.

Top5 A375 cells that have not undergone constricted migration through 5µm pores even after 10 chances to do so.

Bottom5 A375 cells that have undergone constricted migration through 5µm pores for 10 rounds.

Top20-5 A375 cells that have not undergone constricted migration through 5µm pores even after 20 chances to do so.

Bottom20-5 A375 cells that have undergone constricted migration through 5µm pores for 20 rounds.

Top-12 A375 cells that have not undergone migration through 12µm pores even after 10 chances to do so.

Bottom-12 A375 cells that have undergone migration through 12µm pores for 10 rounds.

Results

Melanoma cells exhibit an increase in migration efficiency and morphological changes after multiple rounds of constricted migration

To investigate whether the 3D genome organization is affected by constricted migration, we performed sequential rounds of constricted migration (through 5-µm pores in Transwell filters) on A375 cells (Figure 1A, see STAR Methods for a detailed experimental design). Interestingly, cells that successfully undergo constricted migration through 5-µm pores migrate more efficiently in subsequent rounds of the same Transwell assay. As a result, the population of cells derived from those that have passed through the 5-µm pores for 10 consecutive rounds (Bottom-5) migrate at high efficiency (~70%) as compared to the initial population (20%) (Figure 1B*i* and Figure S1A). In contrast, cells that have failed to undergo constricted migration through 5-µm pores show a progressive decrease in migratory efficiency, approaching 0% migration after 10 rounds (Top-5) (Figure 1B*i* and Figure S1A). The differences in migration efficiency correspond to other notable differences in cell phenotype. Phase contrast imaging of the subpopulations shows that Bottom-5 cells exhibit a decrease in cell-cell adhesions and an elongated cell body (suggesting a more mesenchymal phenotype) when compared to Top-5 cells (Figure 1B*ii* and Figure S1C). These morphological characteristics and migration efficiency differences are maintained even after continuous passage or multiple freeze-thaw cycles, indicating stable phenotypes among Top-5 and Bottom-5 cells (Figure S1B). Live cell imaging of Top-5 and Bottom-5 cells migrating on a 2D surface shows that Bottom-5 cells maintain their elongated shapes and display lobopodia/lamellipodia-like migration, while Top-5 cells display amoeboid-like migration over a 13-hr migration period (Figure 1B*iii* and Movie S1 and S2). These results indicate that the changes (morphological and/or genetic) associated with passing through constrictions fosters migration in consecutive rounds. These phenotypes are consistent with previous studies showing that the degree of invasiveness is often correlated with changes in mechanical properties of cells and increase of cell shape irregularity (Lyons et al., 2016, Machesky, 2008).

It has been previously reported that A375 cells are heterogeneous in their metastatic ability (Kozlowski et al., 1984), so it is possible that the differences we observe are associated only with ability to migrate and are not specific to passing through a constriction. To investigate whether the need to pass through a constriction smaller than the nucleus contributes to the differences in migratory ability that we observed among Top-5 and Bottom-5 cells, we repeated the sequential migration experiment using transwell filters with 12-µm pores. Migration through 12-µm pores

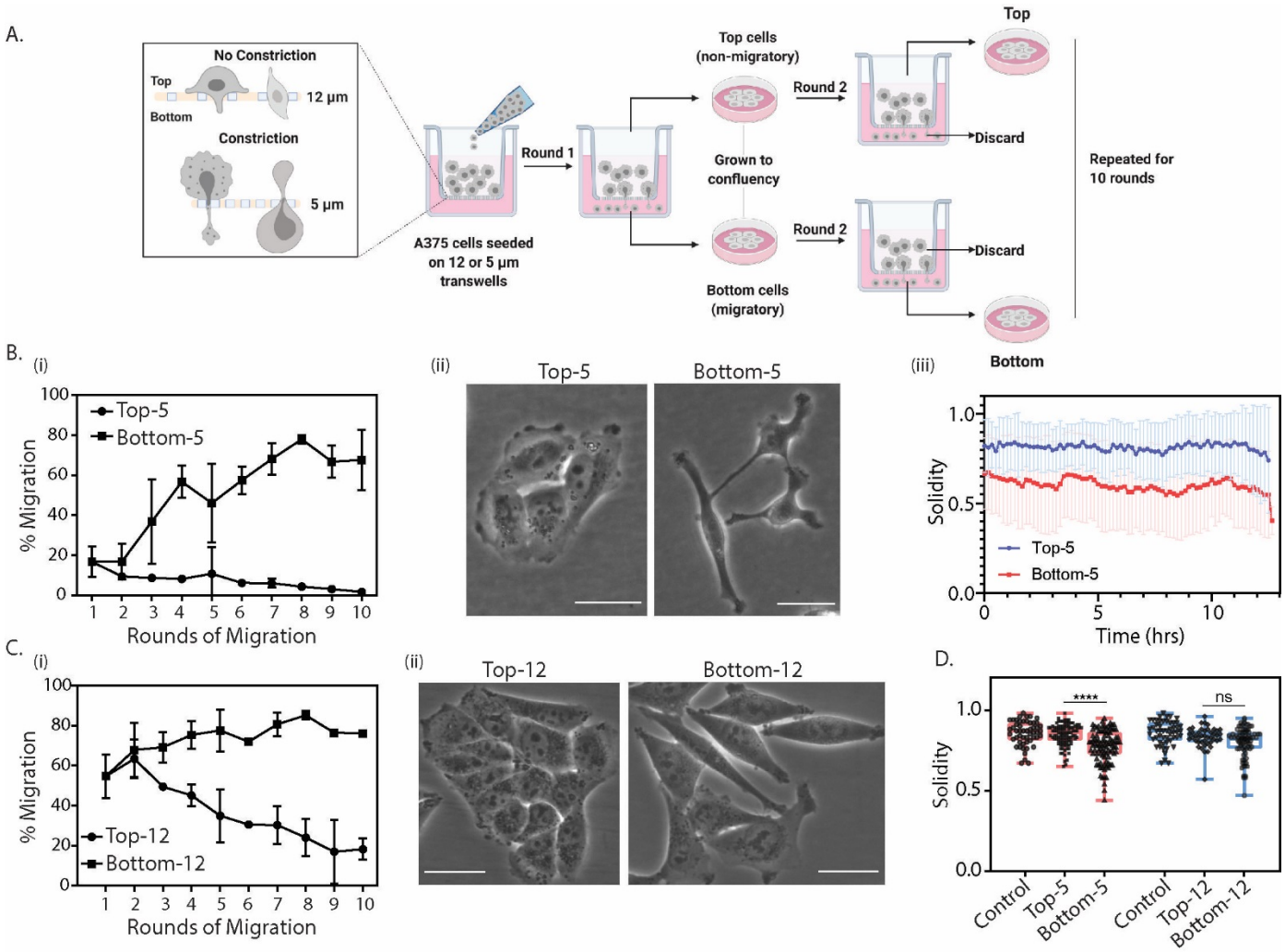

Figure 1. A375 cells exhibit morphological changes and increase in migration efficiency after constricted migration. (A) Overview of sequential transwell migration experiment with A375 cells. (B) (*i*) Migration efficiency (% of cells that migrated through filter pores in each round) of A375 cells during constricted migration (5-µm transwell pore size). Error bars = mean ± SD for n = 3 biological replicates. (*ii*) Phase contrast imaging of A375 cells that have not (Top-5) or have (Bottom-5) undergone 5-µm constricted migration. (*iii*) Solidity measurements of A375 cells undergoing live-cell migration on a 2D surface (1 indicates ideally round and lower values indicate more divergence from round shape). Error bars = mean ± SD for n = 76 Top10 cells and n = 77 Bottom10 cells ($p < 0.0001$, two-tailed t-test). (C)(*i*) Migration efficiency of A375 cells undergoing migration with no constriction (12-µm transwell pore size). (*ii*) Phase contrast imaging of A375 cells that have not (Top-12) or have (Bottom-12) undergone 12-µm transwell migration. (D) Comparison of solidity measurements between A375 cells that have undergone migration through 5-µm and 12-µm pores. Box and whiskers plot showing all data points in Control (n = 52 cells), Top-5 (n = 99 cells), Bottom-5 (n = 98 cells), Top-12 (n = 43 cells) and Bottom-12 (n = 82 cells) (****$p < 0.0001$, ns $p = 0.0726$, two-tailed t-test). Scale bars (white) indicate a length of 25µm.

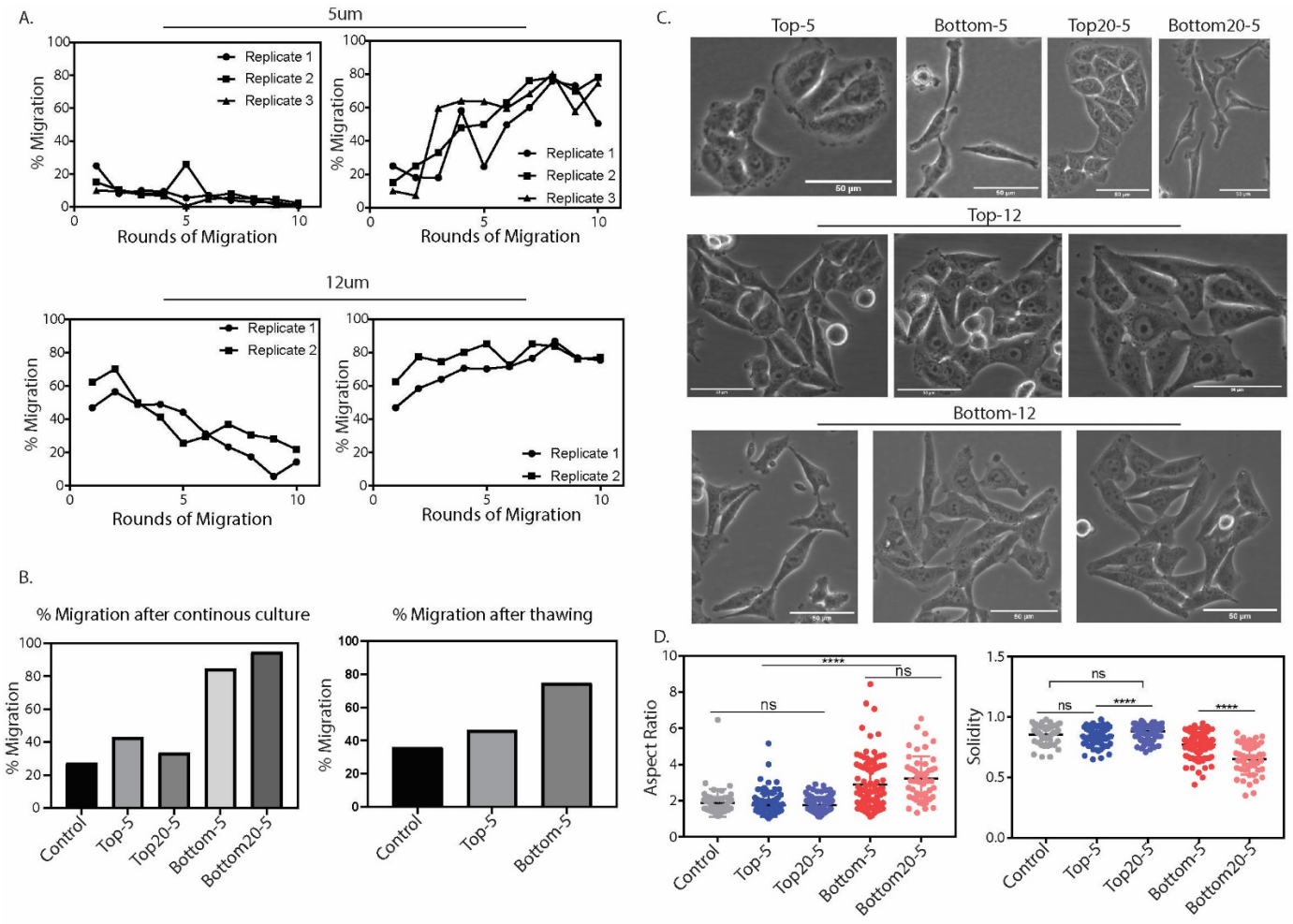

Supplementary Figure 1. A375 cells exhibit persistent increase in migration efficiency and morphological changes after 5-µm constricted migration. (A) Migration efficiency of each replicate for 10 rounds of 5-µm (top graphs) and 12-µm (bottom graphs) transwell migration. (B) Migration efficiency of A375 cells after continuous culture (left graph) and after thawing (right graph). (C) Phase contrast images of A375 cells exposed to 5-µm (top panel) and 12-µm (middle and bottom panels) transwell migration. Scale bars (white) indicate a length of 50 µm. (D) Aspect ratio (left graph) and solidity (right graph) measurements of cells in A375 subpopulations that have undergone 10 rounds (Top-5 and Bottom-5) and 20 rounds (Top20 and Bottom20) of migration through 5µm constrictions (**** $p < 0.0001$; Control (n = 52), Top-5 (n = 99), Top20-5 (n = 93), Bottom-5 (n = 98), Bottom20-5 (n = 48); two – tailed t-test).

does not pose a major spatial barrier for the nucleus since the minimum diameter of the majority of A375 cells is smaller than the 12-µm diameter of the pore (Figure S2A). Accordingly, A375 cells migrate at a much higher rate in the 12-µm pores (~ 55-70 %) in the first round (Figure 1C*i*). Strikingly, cells that were successful at migrating through 12-µm pores (Bottom-12) in each round displayed only a minimal increase in migratory efficiency as compared to the more dramatic increase shown by Bottom-5 cells. In contrast, cells that failed to migrate through the 12-µm pores (Top-12), displayed a significant decrease in migration efficiency after 10 sequential rounds of migration (Figure 1C*i*). This result demonstrates that there is a subset of

cells (Top-5) in the initial population that cannot migrate even through a large pore, but also suggests that larger changes occur after constricted migration, compared to unconstricted. Phase contrast imaging revealed that Top-12 cells display high cell-cell adhesion and more epithelial like phenotypes (like Top-5) when compared to Bottom-12 cells, which show a decrease in cell-cell adhesion and more elongated phenotypes (Figure 1C*ii* and Figure S1C). However, when quantifying solidity or aspect ratio (Figure S1D) over a population average for all A375 sub-populations, it becomes clear that Bottom-5 cells exhibit more dramatic elongated phenotypes compared to Bottom-12 cells which show no significant difference compared to the Control, Top-5 and Top-12 cells (Figure 1D). When challenged to migrate through 5-µm pores, Bottom-12 cells showed a migration efficiency similar to the control population (~ 3-20 %). This suggests that one layer of heterogeneity in the A375 population distinguishes cells that cannot migrate (Top-12) from those that can, but that additional features are required for constricted migration that are not necessarily already present in the Bottom-12 subset of cells. We next turned to investigating the nucleus and chromosome structures of these different sub-groups of cells.

Peripheral localization of heterochromatin and irregular distribution of Lamin A/C correlate with an increased rate of constricted migration

Changes in nuclear morphology are consistently used as a diagnostic tool in cancers (Kadota et al., 2012). Further, it has been reported that, during cancer cell constricted migration, the nuclear envelope can rupture (Denais et al., 2016), blebs can form, and DNA damage can occur (Irianto et al., 2017a, Davidson and Lammerding, 2014). However, it is not clear how these morphological changes might affect the underlying 3D structure of the chromosomes. As noted earlier, lamin content and chromatin state have been implicated in constricted migration and nucleus stiffness. Therefore, we first looked at nucleus structure by immunofluorescence imaging of Lamin A/C and heterochromatin (H3K9me3). While we did not observe differences in nuclear morphology among the migratory and non-migratory cells on average (Figure S2B), in agreement with previous reports showing that the morphological changes with constriction (nuclear blebs, DNA damage) are reversible (Irianto et al., 2017a), we aimed to investigate whether irreversible differences exist among A375 cells with different migratory ability. High resolution confocal microscopy of immunostained A375 Control, Top-12 and Top-5 nuclei revealed a uniform distribution of Lamin A/C throughout the nuclear envelope (Figure 2A, middle panel). In contrast, Bottom-5 nuclei display an altered distribution of Lamin A/C with specific regions of the nuclear envelope devoid of it (Figure 2A and 2B, indicated by white arrow, Movie S3 and S4). The radial distribution of Lamin A/C across the populations of cells is not quantitatively different on average, however (Figure 2B, bottom panel), indicating that the regions devoid of Lamin A/C are specific to each nucleus in Bottom-5 cells. In contrast, Lamin A/C seems to be uniformly distributed in Bottom-12 nuclei with occasional folds of the nucleus (Figure 2A), suggesting that the irregular distribution of Lamin A/C in Bottom-5 nuclei could be a result of constricted migration.

Heterochromatic foci are distributed throughout the nucleus in Control, Top-12 and Top-5 cells (Figure 2A, right panel) with some foci localized to the nuclear periphery, in agreement with previous reports investigating the role of heterochromatin in maintaining the integrity/roundness of the nucleus (Gerlitz and Bustin, 2010, Stephens et al., 2019). In contrast, heterochromatin foci in Bottom-5 nuclei appear to be more dispersed and the majority of signal is localized to the nuclear periphery (Figure 2A, indicated by white arrow). Indeed, quantifying the radial distribution of H3K9me3 signal in the nucleus reveals that Bottom-5 nuclei display a lower H3K9me3 intensity in the interior of the nucleus and an increase in intensity at the periphery when compared to Control, Top-5 or cells from 12-µm transwell migration (Figure 2C).

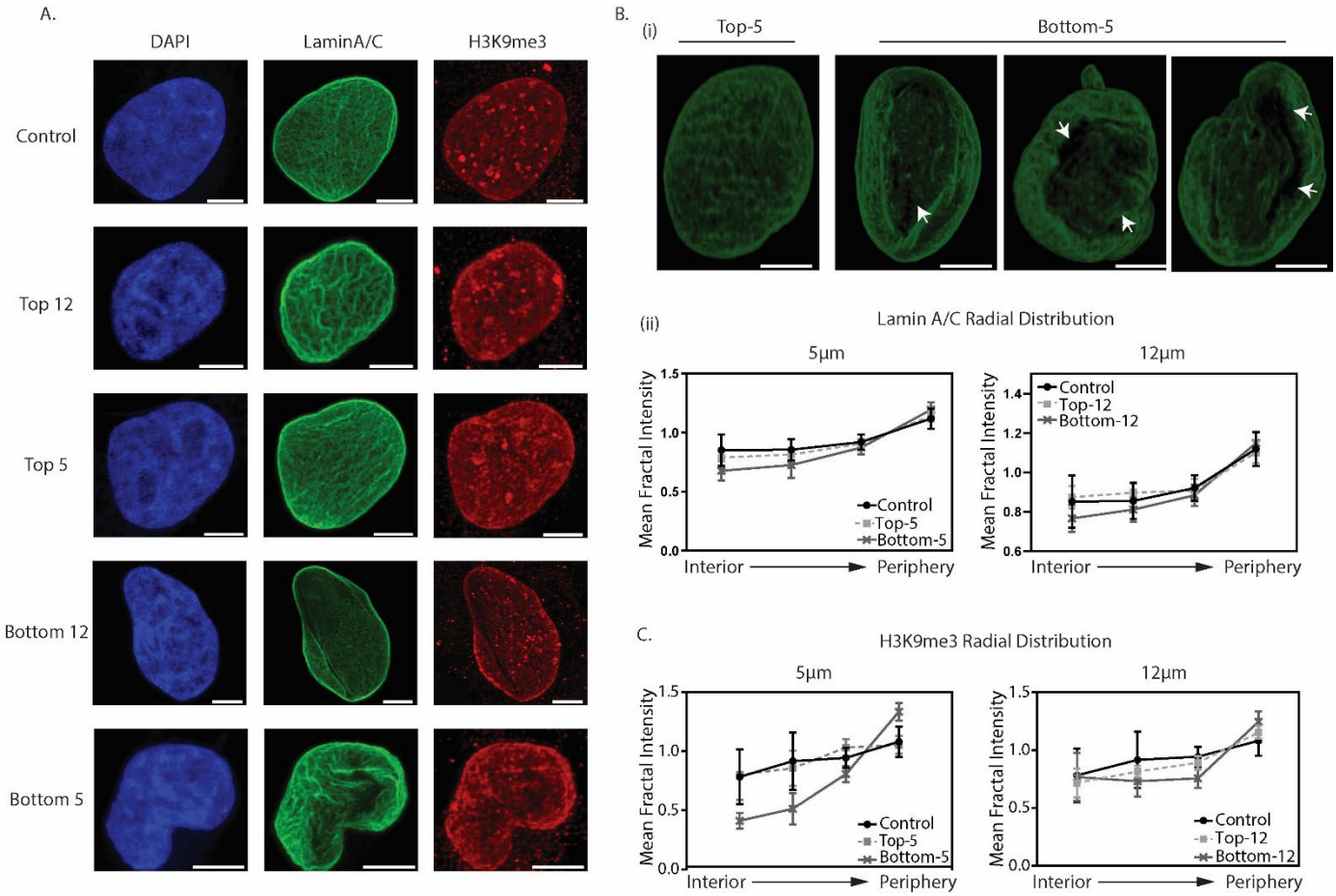

Figure 2. Irregular distribution of Lamin A/C and heterochromatin upon constricted migration. (A) A375 nuclei stained with DAPI (blue), Lamin A/C (green) and H3K9me3 (Red) in the indicated migration conditions. Images shown are the max projection of z-stacks. (B) (*i*) A375 Bottom-5 nuclei stained for Lamin A/C exhibit areas devoid of Lamin A/C after constricted migration (white arrows). Images shown are snapshots of 3D reconstruction of z-stacks using Leica 3D analysis software. For full 3D visualization see Movie S3 and S4. (*ii*) Radial distribution of Lamin A/C in A375 cells that have undergone 5-µm or 12-µm transwell migration. (C) Radial distribution of H3K9me3 in A375 cells that have undergone 5-µm and 12-µm transwell migration. Error bars = mean ± SD of n=25 nuclei for each condition. All scale bars (white) indicate a length of 5µm.

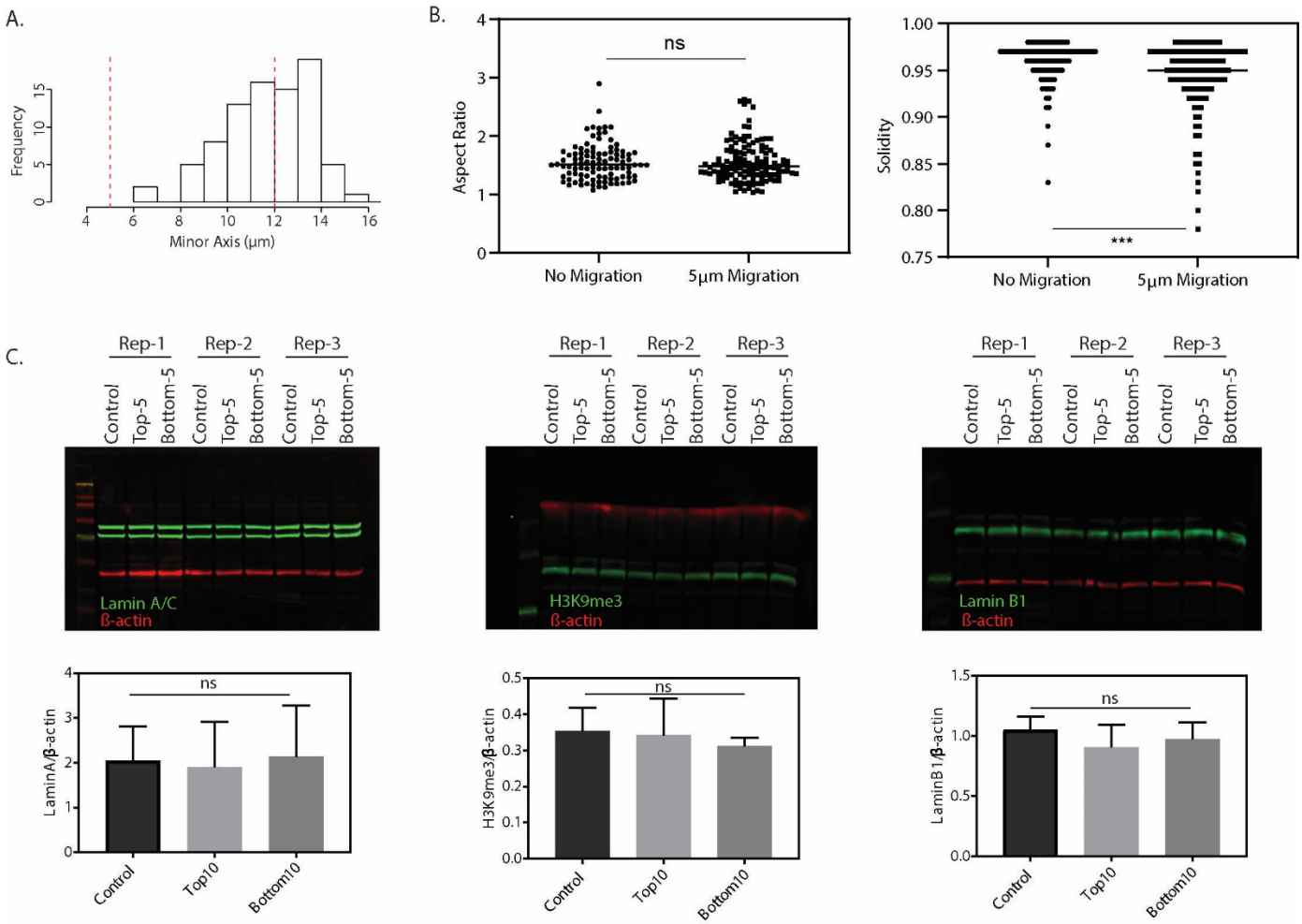

Supplementary Figure 2. Nuclear morphology is not dependent on lamin levels or heterochromatin levels. (A) Minor axis (minimum diameter) measurements of A375 cell nuclei based on confocal z stacks. N=85. (B) Measurements of Aspect Ratio (left graph) and Solidity (right graph) of A375 nuclei that have not undergone constricted migration (N=100) and nuclei that have undergone 5-µm constricted migration (N=128). Mann-Whitney test performed for both Aspect Ratio (p-value = 0.748) and Solidity (p-value = 0.0003). (C) Western blot analysis of A375-Control, Top-5 and Bottom-5 cells probing for Lamin A/C (left panel), H3K9me3 (middle panel) and Lamin B1 (right panel). Two-tailed t-test performed; p-values not significant for any of the probed proteins.

Interestingly, Lamin A/C and H3K9me3 protein levels remain the same across all A375 subpopulations as revealed by Western blot (Figure S2C). This is in contrast to other reports that suggest lower levels of Lamin A/C increase the ability to undergo constricted migration (Harada et al., 2014). Our observations imply that, in A375 cells, constricted migration proficiency is related to the distribution of Lamin A/C and heterochromatin, instead of total protein levels. Given the role of lamins and heterochromatin in organizing the 3D genome structure, we next asked whether related changes are found in the 3D organization of chromosomes.

Genomic regions change their compartmentalization after rounds of constricted migration

To measure changes in genome wide chromosomal contacts, we performed genome-wide chromosome conformation capture (Hi-C) on Control, Top-5, Bottom-5, Top-12 and Bottom-12 cells (see STAR Methods and Table S1 for processing and statistics). Strikingly, using 250kb binned matrices, we observe regions of the genome that switch their compartment identity specifically in Bottom-5 cells but not in any of the other conditions (Figure 3A, example compartment switch indicated by black arrow). We then performed Principal Component Analysis (PCA) to classify regions according to A/B compartment identity. We identified regions of the genome that have a consistent compartment identity among all un-constricted conditions (Control, Top-12, Top-5, Bottom-12) but change compartment identity (A to B or B to A) in Bottom-5 cells (Figure 3B, highlighted region, for example). We determined that 1% of 250 kb regions across the genome switched from the B (typically more heterochromatic) to A (typically more euchromatic) compartment and about 2% of the 250Kb bins switched from A to B compartment in Bottom-5 cells (Figure 3C). We observed a comparatively very small number of compartment identity switches in all the other conditions (Figure 3C) implying that 3D genome structure changes could be specific to constricted migration. We also extended migration through 5-µm pores up to 20 rounds (Bottom20-5) and observe similar compartment patterns and compartment identity switches, reinforcing the idea that these specific rearrangements of the genome results/are related to constricted migration (Figure 3C and S3).

Even though most compartment switches were specific to Bottom-5 cells, we investigated the distribution of PC1 values of the regions that switched compartments in Bottom-5 among all the A375 conditions (Figure 3D). Regions of the genome that were previously in the B compartment in Control cells and switch to the A compartment in Bottom-5 cells show a negative distribution of PC1 values in non-migrating cells (Top-12 and Top-5), consistent with a B compartment identity, similar to the Control. As expected, the PC1 distribution switches to a positive mean in cells that have undergone constricted migration (Bottom-5 and Bottom20-5) (Figure 3D*i*). However, while Bottom-12 cells exhibit a negative PC1 mean (still maintaining their original B compartment identity), it is less negative when compared to Control and Top cells (Figure 3D*i*). A similar pattern is observed in regions of the genome that switch compartment identity from A to B type. While the mean of PC1 distribution is positive for Control and Top cells and negative for Bottom-5 and Bottom20-5 cells, Bottom-12 cells exhibit a less positive mean of PC1 distribution (Figure 3D*ii*). This observation could imply that shifts in genome structure begin to happen in cells that undergo migration with minor nucleus deformations, but are more dramatic with a narrow constriction, or that the Bottom-12 cell population contains some cells already primed for confined migration.

Not only are compartment changes a visually apparent difference in constricted migrating cells, but also genome-wide hierarchical clustering analysis of the compartment eigenvectors segregates conditions according to whether they have undergone constricted migration or not, indicating that the changes in chromatin compartmentalization are directly linked to migratory ability (Figure 3E). Given our observations on the increased peripheral localization of H3K9me3 distribution after confined migration (Figure 2), we sought to investigate whether genomic regions that change

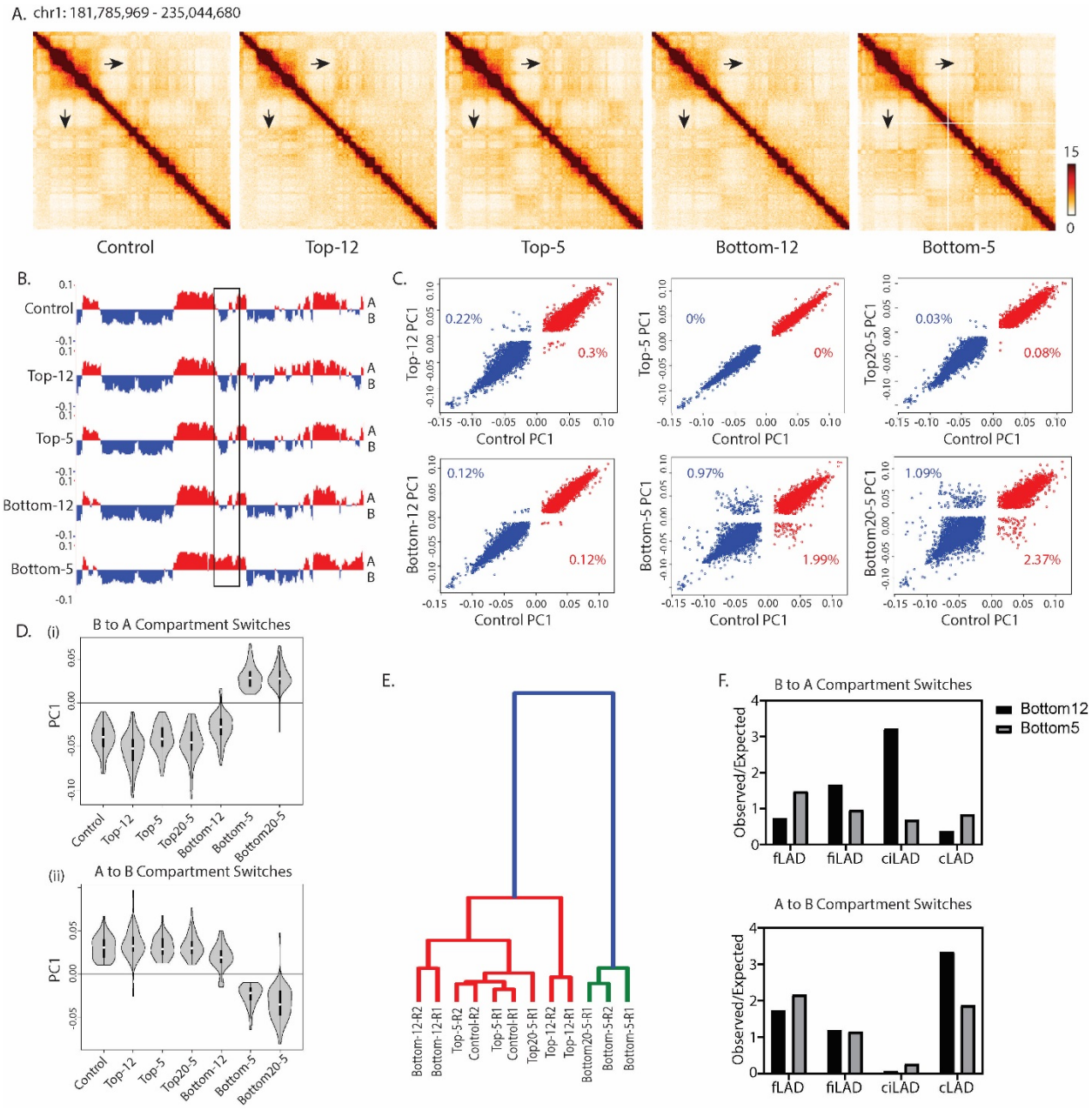

Figure 3. Compartment identity switches observed after constricted migration. (A) 250Kb binned Hi-C interaction heatmaps of chr1 (chr1: 181,785,969 - 235,044,680) among all A375 subpopulations. Arrow indicates region of visible compartment change. (B) PC1 track of compartment identity in the same region of chr1 among all A375 subpopulations. Compartment tracks are binned at 250Kb. Boxed region highlights to one of several compartment switches in this region, the same switch highlighted by arrows in (A*)*. (C) Correlation between A375 Control PC1 with A375 cells that did not undergo transwell migration (top three panels) and A375 cells that did undergo transwell migration (bottom three panels). Percentage of bins that met the criteria for "compartment switch" from B to A (blue) or A to B (red) indicated on each panel. (D) Distribution of PC1 values across all A375 subpopulations for the regions that switched their compartment identity from B to A compartment (*i*) and A to B compartment (*ii*) in Bottom-5 cells. (E) Clustering of all A375 subtypes by their compartment PC1. (F) Observed/Expected representation of different LAD types in regions that switch their compartments from B to A and A to B in Bottom-5 cells.

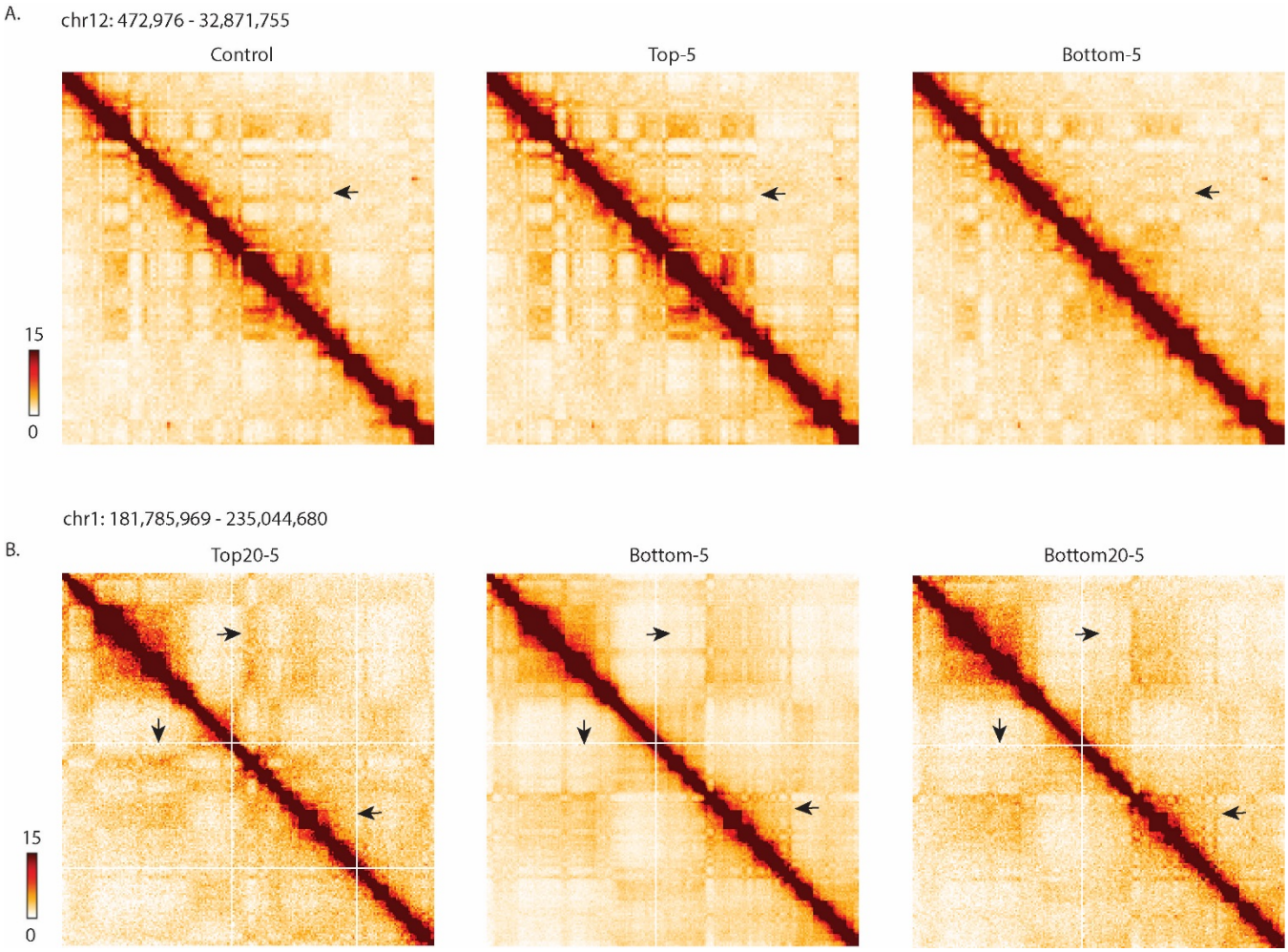

Supplementary Figure 3. Compartment identity switches persist after 20 rounds of 5-µm constricted migration. (A) Hi-C interaction heatmap of chr12 binned at 250Kb in A375-Control, Top-5 and Bottom-5. (B) Hi-C interaction heatmaps of chr1 (same chromosomal location as Figure 3A) in A375 cells that have undergone 20 rounds of 5-µm transwell migration. Black arrows indicate regions that exhibit changes in compartment profiles upon migration through 5-µm constrictions.

compartment identity correspond to certain lamin association types. We used a previously established LAD atlas (Kind et al., 2015) across a cohort of nine different cell types that classify LADs as: cLADs (constitutive LADs; regions associated with the nuclear lamina in all cell types), ciLADs (constitutive inter LADs; regions located in the interior of the nucleus across all cell lines), fLADs and fiLADs (facultative LADs and facultative inter LADs; regions that are sometimes associated with the nuclear lamina across the cell types). We observed that regions that switched their compartment identity after constricted migration (Bottom-5) were enriched in fLADs both in B to A (Figure 3F*i*) and A to B (Figure 3F*i*) switches. The high incidence of compartment changes in fLAD regions might relate to the inherently bivalent state of fLADs, representing their ability to transition between lamina-association and dissociation. Additionally, Bottom-12 and Bottom-5 presented with an enrichment of cLADs in the regions that switch from A to B compartment,

suggesting a possible further spatial consolidation of heterochromatin regions corresponding to the coalescence of H3K9me3 at the nuclear periphery.

Interestingly, we observed an over-representation of ciLADs in regions switching their identity from B to A compartment between Top-12 and Bottom-12 (Figure 3F*i*). Given that ciLADs are regions that do not associate with the nuclear lamina in all the examined cell types, we did not expect these regions to be in the B-compartment in the non-migratory cells. We have identified 96 bins that are classified as ciLADs residing in a B compartment in Top-12 cells but are found in the A compartment in all other conditions. Gene ontology enrichment analysis identified functions correlating to cell motility and the regulation of actin cytoskeleton for the genes found in these regions. Additionally, we also observed an over-representation of cLADs in regions that switched their compartment identity from A in the Top-12 to B in Bottom-12, encompassing 253 bins found in the A compartment in Top-12 and in the B compartment in all the other conditions. The genes in these regions were associated with melanogenesis and neuronal pathways. Taken together, these observations suggest that Top-12 cells (the least migratory in the constricted migration spectrum) harbor a 3D genome structure that separates them from the highly migratory cells (Bottom-5 and Bottom20-5) and likely reflects maintenance of melanocyte identity.

Gene expression changes after constricted migration reflect metastatic potential

To investigate potential changes in gene expression in cells that have undergone constricted migration, we performed RNA-Seq on all A375 subpopulations. We identified 977 and 1473 genes that were differentially expressed in Bottom-5 and Bottom20-5, respectively (Figure S4A and Table S2). Hierarchical clustering of all conditions, starting with the subset of genes differentially expressed in Bottom-5 or Bottom20-5, revealed that cells that undergo constricted migration cluster separately from all other conditions (Figure 4A and Figure S4B). Overall, we observe three major gene clusters: cluster 1 included 482 genes that are upregulated in Bottom-5 and Bottom20-5 but seem to be mostly downregulated in all other cells. Pathway enrichment analysis identified upregulated pathways related to metastasis, such as TGF-beta, TNF-alpha, EGFR and Integrin β-4 signaling pathways (Figure 4B*i*). On the other hand, cluster 2 included 368 genes that were downregulated in Bottom-5 and Bottom20-5 but upregulated among all other cells. Interestingly, enriched pathways are involved in developmental pathways such as neural development. Since melanoma cells originate from neural crest, these observations suggest that this cluster relates to melanocyte specific gene expression (Figure 4B*ii*). Finally, cluster 3 included 533 genes that were downregulated in Bottom20-5 and upregulated in Top-5 (Figure 4A). Some of these genes relate to cell adhesion, perhaps related to the differences we observe in cell-cell contacts between these subsets (Figure 1B).

These gene expression changes correlate with A/B compartment changes upon constricted migration (Fig. 4C). Genes found in regions that switch their compartment identity from A to B in Bottom-5 or Bottom20-5 cells display an overall decrease in expression when compared to all other conditions (Figure 4C*i*). Similarly, genes found in regions that switch their identity from B to A compartment in Bottom-5 and Bottom20-5 cells display an overall increase in expression (Figure 4C*ii*). This result suggests that some of the compartment changes after confined migration directly relate to changes in gene regulation. We cannot definitively say whether certain key

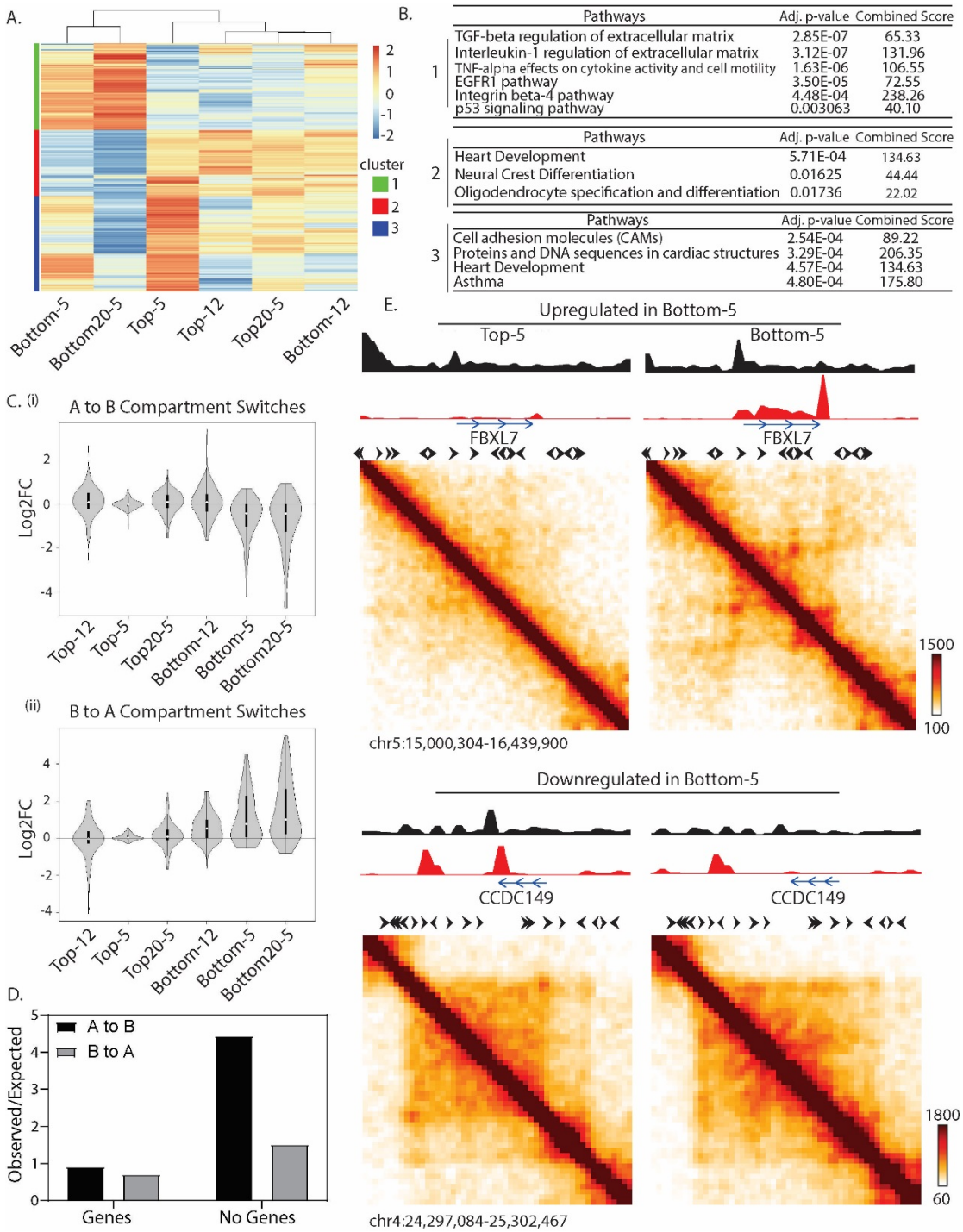

Figure 4. Changes in gene expression correlate with metastatic ability and chromosome structure changes. (A) Hierarchical clustering of RNA-Seq datasets based on differentially expressed genes of Bottom-20 cells. (B) Pathway enrichment analysis of identified gene clusters from (A) using BioPlanet 2019 package from Enrichr. (C) Log2FC of expression in the indicated condition vs. Control for genes located in regions that switch compartments from A to B (*i*) and B to A (*ii*) in Bottom-5 cells. (D) 20Kb binned Hi-C matrices of upregulated (FBXL7) and downregulated (CCDC149) genes in Bottom-5 cells. Tracks over the matrices represent ATAC-Seq (black) and RNA-Seq (red). The tracks have been smoothed with 40Kb bins. Black arrows indicate known CTCF motif sites. (E) Observed/Expected representation of regions that switched from A to B compartment based on the presence or absence of genes within the bin.

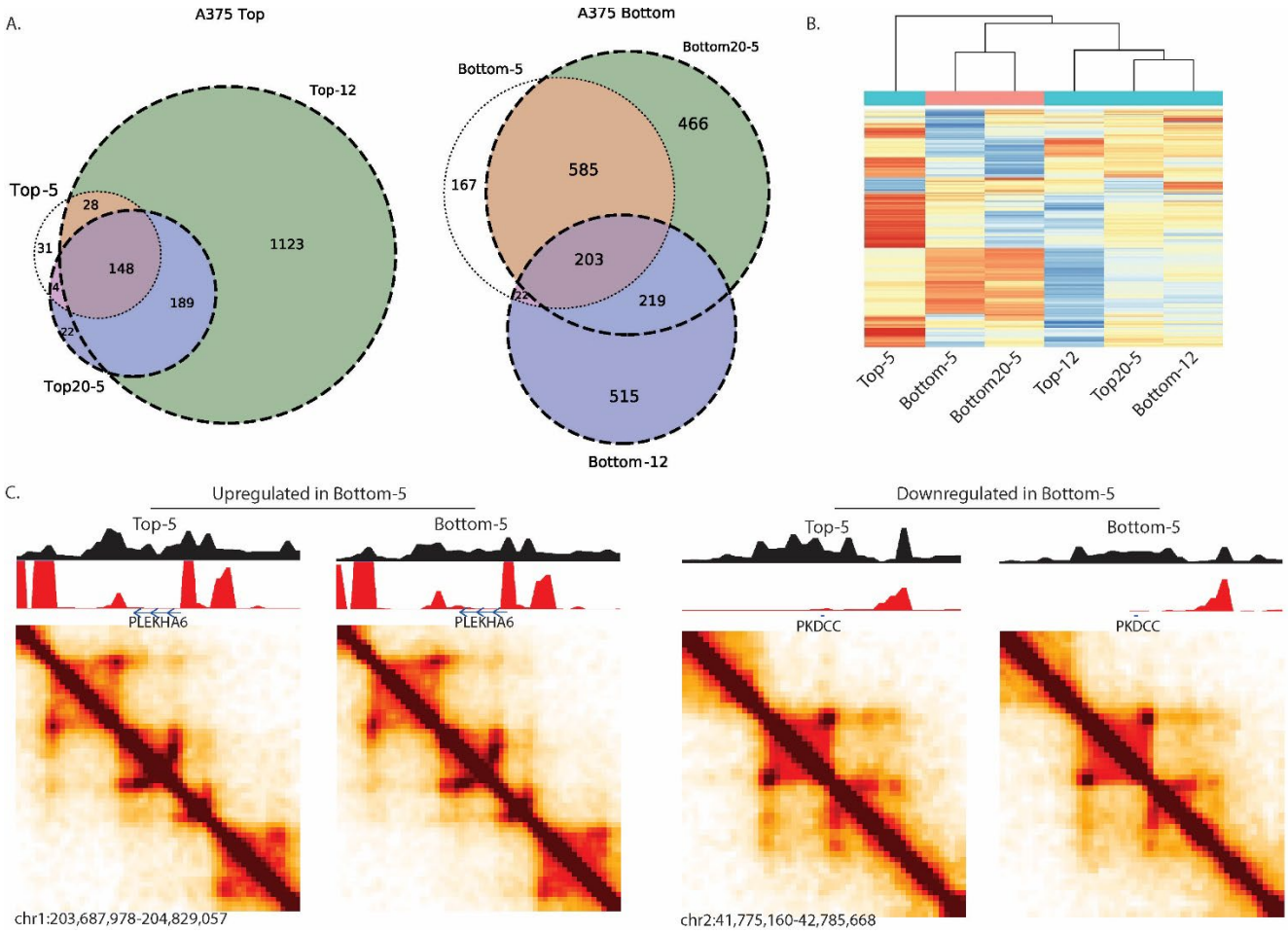

Supplementary Figure 4. Gene expression profile separately clusters cells that have undergone constricted migration (Bottom-5 and Bottom-20) from all other A375 subpopulations. (A)Venn diagram displaying differentially expressed genes in all A375 populations that did not undergo constricted migration (left panel) and cell that underwent 5-µm constricted migration (right panel). (B) Hierarchical clustering of all A375 subset of cells based on genes that are differentially expressed in Bottom-5 cells. (C) Hi-C contact matrices binned at 20Kb and smoothed at 40Kb bin size of upregulated genes (PLEKHA6, left two panels) and downregulated genes (PKDCC, right two panels) in Bottom-5 cells. Black track represents ATAC-Seq signal while the red track represents RNA-Seq signal.

migration genes were, for example, already active and in the A compartment in a subset of A375 control cells, and these were selected by sequential migration, or whether some such genes became active after a compartment switch was induced by confined migration. However, we can conclude that at least part of the underlying biological function of the compartment switching we observe in confined migrating cells involves changes in gene expression. Interestingly, we found that a large proportion of the genomic bins that switch from A to B and B to A compartment contain no genes; fold enrichment of 4 and ~2, respectively (Figure 4D). This observation indicates that a substantial portion of structural changes after migration must be explained by something other than gene regulation changes. We hypothesize that these regions might change as a result of or to accommodate the physical strain on the chromatin fiber during constricted migration.

Additionally, to investigate whether the observed gene expression changes related to local genome structure changes, we zoomed in to regions of the genome encompassing some of the highest upregulated or downregulated genes after constricted migration (Figure 4E). We initially explored genes that were upregulated (log2FC > 1) in cells that had undergone constricted migration (Bottom-5 and Bottom20-5). When zooming in to the FBXL7 gene (~ 8-fold upregulated in Bottom-5 and Bottom20-5), we observed the emergence of a domain-like structure in Bottom-5 cells and an increase in chromatin accessibility (Figure 4E, first panel). Similarly, when exploring genes that were downregulated after constricted migration (Bottom-5 and Bottom20-5), we found genes whose local 3D structure was altered in Bottom-5 or Bottom20-5 cells with the disappearance of the loop present in Top-5 and a decrease in chromatin accessibility (SOD3 and CCDC149 3-15 fold downregulated; Figure4E, second panel). However, we also encountered cases in which the genes were differentially expressed such as PLEKHA6 (log2FC > 2 in Bottom-5 and Bottom20-5) and PKDCC (log2FC = -2.5 in Bottom-5 and Bottom-20) but their local genomic structures remained similar with modest changes in chromatin accessibility (Figure S4C). We observe that the loss or formation of loops or domains associated with changes in transcription occurs in regions that had few or no other strong architectural loops, such as the kind mediated by CTCF. Genes that change expression without notable 3D looping changes, in contrast, were located in regions with many other loops and TAD boundaries. These observations support the idea that transcription driven domains can arise separately from CTCF-based domains (Rowley et al., 2017). Further, the transcription-associated CCDC149 loop occurs between an existing TAD boundary and a promoter, and could be explained by a collision between opposing direction loop extrusion and RNA polymerase activity, as suggested in other systems (Brandao et al., 2019).

Inter-compartment interactions increase after constricted migration

While the switching of compartment identity after confined migration is a striking phenomenon, and clearly apparent by visual inspection of the contact maps, quantitatively, only ~ 3% of the genomic bins (250Kb bins) were affected by a complete compartment switch according to our thresholds. To evaluate how constricted migration impacted the rest of the chromosome contacts, we evaluated contacts not involved in compartment identity switches by reordering the 250Kb binned matrices from the strongest B to strongest A bins based on PC1 values (Figure 5A) (Imakaev et al., 2012). We observe an evident separation between the B and A compartment in all subpopulations of A375 arising from 5µm (Figure 5A*i* and Figure S5A) and 12µm (Figure 5A*ii* and Figure S5A) Transwell migration experiments. However, the relative strength of inter and intra-compartment contacts changes between Top and Bottom cells (Figure 5A, middle panels). Bottom-5 cells exhibit a loss in the strongest B-B interactions and an overall increase in interactions between the strongest B and strongest A compartments. This phenomenon has been previously reported in neutrophils after passage through small pores, suggesting it may be a general feature of confined migration genomic structural changes (Jacobson et al., 2018). This change in interaction frequency correlates with changes in gene expression. Regions that exhibit a strong B-B interaction loss display an overall increase in expression of genes found in these regions. Additionally, the expression of genes found in regions that display a gain in B-B interactions show an overall decrease in expression correlating with strengthening of the B-B interactions (Figure S5B). Interestingly, though there is increased mixing of the strongest A and B compartments after confined migration, there is actually increased segregation of regions that are weakly

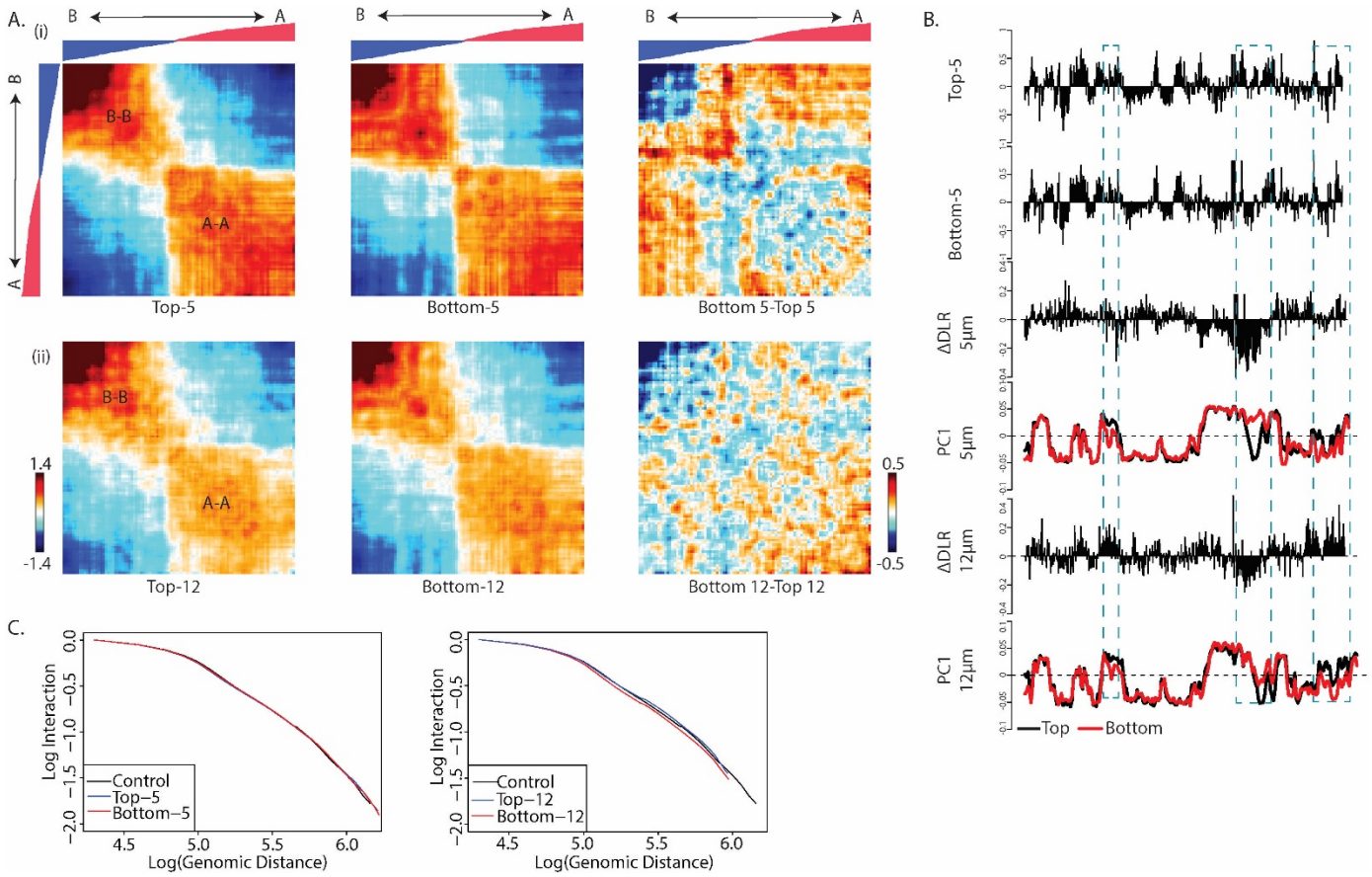

Figure 5. Increase in inter-compartment interactions upon constricted migration. (A) Compartmentalization saddle plots display interaction Z-score (interactions normalized by generic distance decay) between all bin pairs, reordered by PC1 values derived from A375 Control HiC data. Interactions between the strongest B regions are in the upper left corner while A-A interactions are in the lower right corner. The reordered Control PC1 values are displayed over the saddle plots. (B) Along chromosome 1 (chr1:170,000,001–225,000,000), from top to bottom: Distal to local (DLR; 100 kb bins) ratio for Top-5 cells; DLR of Bottom-5 cells; Delta DLR (Bottom-5 – Top5). Positive DLR values indicate a gain of distal interactions (>3Mb) while negative values indicate a loss of distal and gain of local interactions (<3Mb); PC1 values (250 kb bins) of Top-5 (black) and Bottom-5 (red) samples; Delta DLR (Bottom12-Top12); PC1 values of Top-12 (black) and Bottom-12 (red). Positive PC1 values represent A-compartment identity and negative PC1 values B-compartment identity. (C) Whole genome scaling plots at 20Kb bin size comparing A375 cells that have been exposed to 5-μm transwell migration (top plot) and 12-μm transwell migration (bottom).

compartmentalized (eigenvector values near 0) in cells that did not pass through constrictions. It appears that the B compartment bins that were previously ambiguous or near compartment boundaries in Top cells are more strongly associated with the rest of the B compartment after confined migration. We also observe a loss of the strongest B-B contacts in Bottom-12 as compared to Top-12, though this effect is not as strong as in the constricted migration case. In contrast to Bottom-5 cells, Bottom-12 cells exhibit an increase of interactions between A-A contacts relative to Top-12.

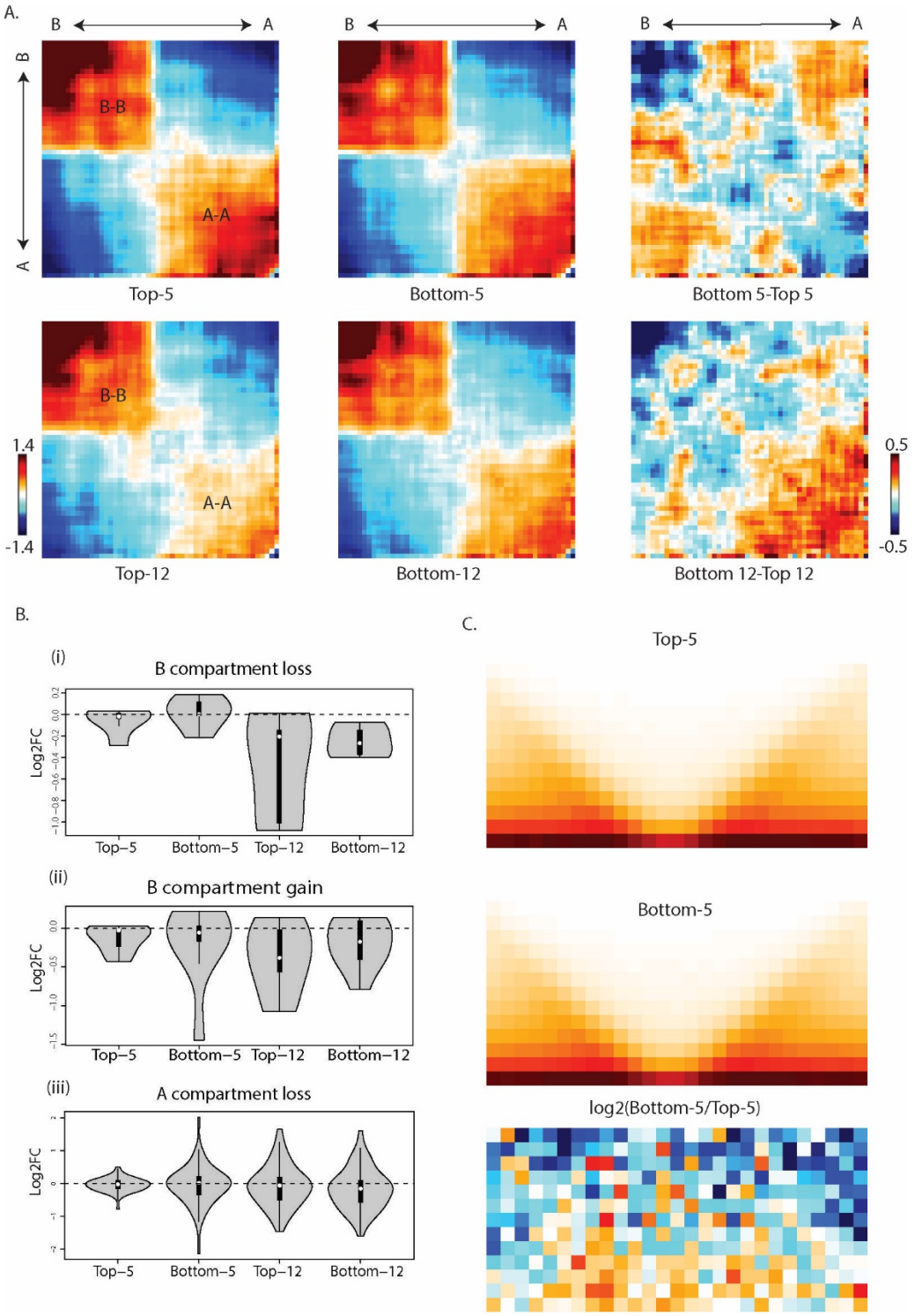

Supplementary Figure 5. Changes in compartment interaction strength correlates with overall gene expression pattern. (A) Saddle plots binned and smoothed using 500Kb bin size for chr18 reordered from strongest B to strongest A compartment. (B) Gene expression changes corresponding to strong B-B interaction loss (i), moderate B-B interaction gain (ii) and A-A interaction loss (iii). (C) Aggregate contact maps (40 kb bins) at TAD boundaries called by the Insulation Score method of cworld-dekker with strength greater than 1 of Top-5 (Top panel) and Bottom-5 (middle panel).

To understand how these differences in compartment interaction frequencies relate to interactions with linearly local or distal chromosome regions, we calculated the distal-to-local ratio (DLR) of Hi-C interaction frequencies (Figure 5B). Here, distal is defined as interactions with regions more than 3 Mb away along the chromosome. This measure has previously been associated with changes in chromosome compaction (Heinz et al., 2018) and is related to a measure used to quantify loss of local chromosome structure with chromosome fiber digestion (Belaghzal et al., 2019). We find that in general, where regions along the chromosome strengthen or switch to A compartments, local interactions increase relative to distal (negative DLR value). Where regions increase their B compartmentalization or lose A identity, distal interactions increase (positive DLR). This could suggest that increased B compartmentalization often occurs when a region is brought closer to other heterochromatin regions far away on the chromosome, perhaps by co-localization at the nuclear lamina, while loss of B/increased A compartmentalization involves breaking distal contacts and increasing local contacts. (highlighted region, Figure 5B).

Although the DLR shows that local and distal interaction patterns of individual regions do change, the local decay of interactions with distance does not change among any of the A375 subpopulations (Figure 5C). This local interaction scaling reflects local chromatin compaction and average local loop size and density, and thus we show that constricted migration does not overall change these local chromosome features. Moreover, we investigated whether constricted migration disrupts TAD boundaries, and we observe no clear differences between any of the conditions (Figure S5C). These observations demonstrate that the major changes upon constricted migration occur in larger scale chromosome structures and are in line with previous reports that TAD-scale interactions are independent from compartment-scale interactions such that one can change without dramatically affecting the other (Nuebler et al., 2018).

Global genomic rearrangements after constriction migration

Constricted migration has previously been shown to result in DNA damage and genome instability (Irianto et al., 2017a). Since Hi-C can detect structural aberrations such as translocations, we examined interchromosomal interactions in 2.5 Mb binned matrices to search for potential genomic aberrations after confined migration (Figure 6).

At first glance, it is evident that translocations inherent to A375 are present in all sub-populations of cells (Figure 6A and S6). However, a new translocation between chr5 and chr13 (t(5;13)) is evident only in cells that had undergone constricted migration (Bottom-5 and Bottom20-5) (Figure 6B and S6). To narrow the specific breakpoint region of this translocation, we focused on Hi-C contact frequency between chr5 and chr13 (Figure S6). While in Top cells (Top-12, Top-5 and Top20-5) contact frequencies between chr5 and 13 remain uniform across the whole chromosome, in Bottom-5 cells we observe a high frequency of interaction between chromosome 5 and chromosome 13 followed by a sudden drop of interactions, indicating the translocation breakpoint (Figure S6). Interestingly, the translocation breakpoint falls in a gene poor region of both chromosomes.

We next used Hi-C contacts to estimate what fraction of the chromosomes in the population contain this translocation (See STAR method for detailed analysis approach). We found that this translocation was only present in 6.13% of chromosomes in Bottom-5 and 2.89% in Bottom-20.

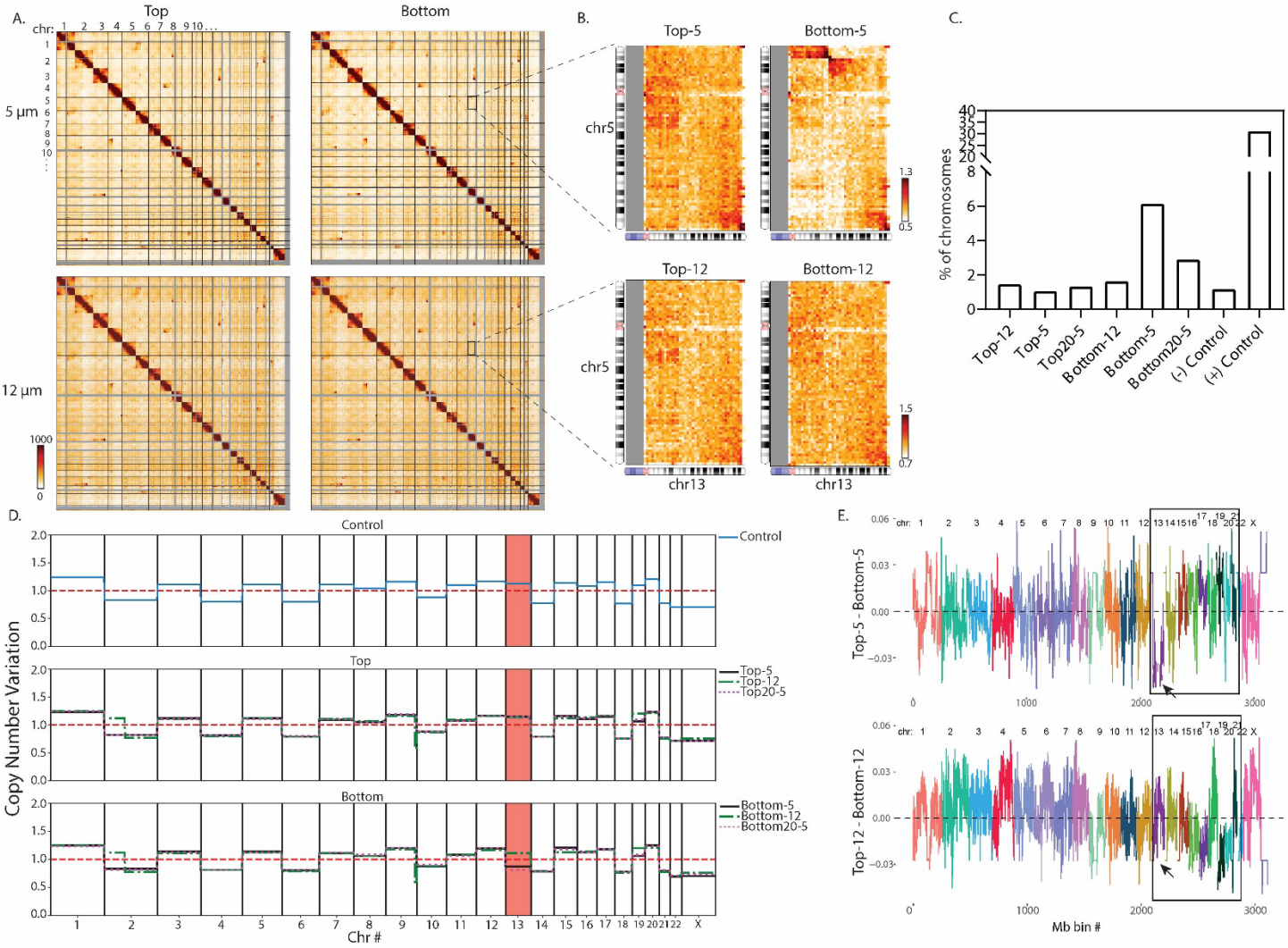

Figure 6. Global genomic rearrangements after constricted migration. (A) Whole genome 2.5Mb Hi-C interaction frequency maps for cells that have undergone 5 and 12-µm transwell migration. (B) Zoom-in of inter-chromosomal interactions between chr5 and chr13 for cells that have undergone 5 and 12-µm transwell migration. (C). Estimation of the % of chromosomes bearing the t(5;13) based on the frequency of the proposed translocation interaction divided by the average neighboring bin cis interactions. (D) Copy number variation among all A375 subtypes inferred from total raw Hi-C counts. Red dashed line represents the mean copy number level while the other lines represent the copy number of A375 cell subpopulations. The region highlighted in red shows that chr13 exhibits copy number loss after 10 rounds of constricted migration. (E) Plots represent the difference in inter-chromosomal fraction (ICF) in cells that have undergone migration through 5-µm constrictions (top plot) and cells that have undergone migration through 12-µm constrictions (bottom plot) using 1Mb binned Hi-C contacts. The boxed region highlights regions of difference between constricted and unconstricted migration.

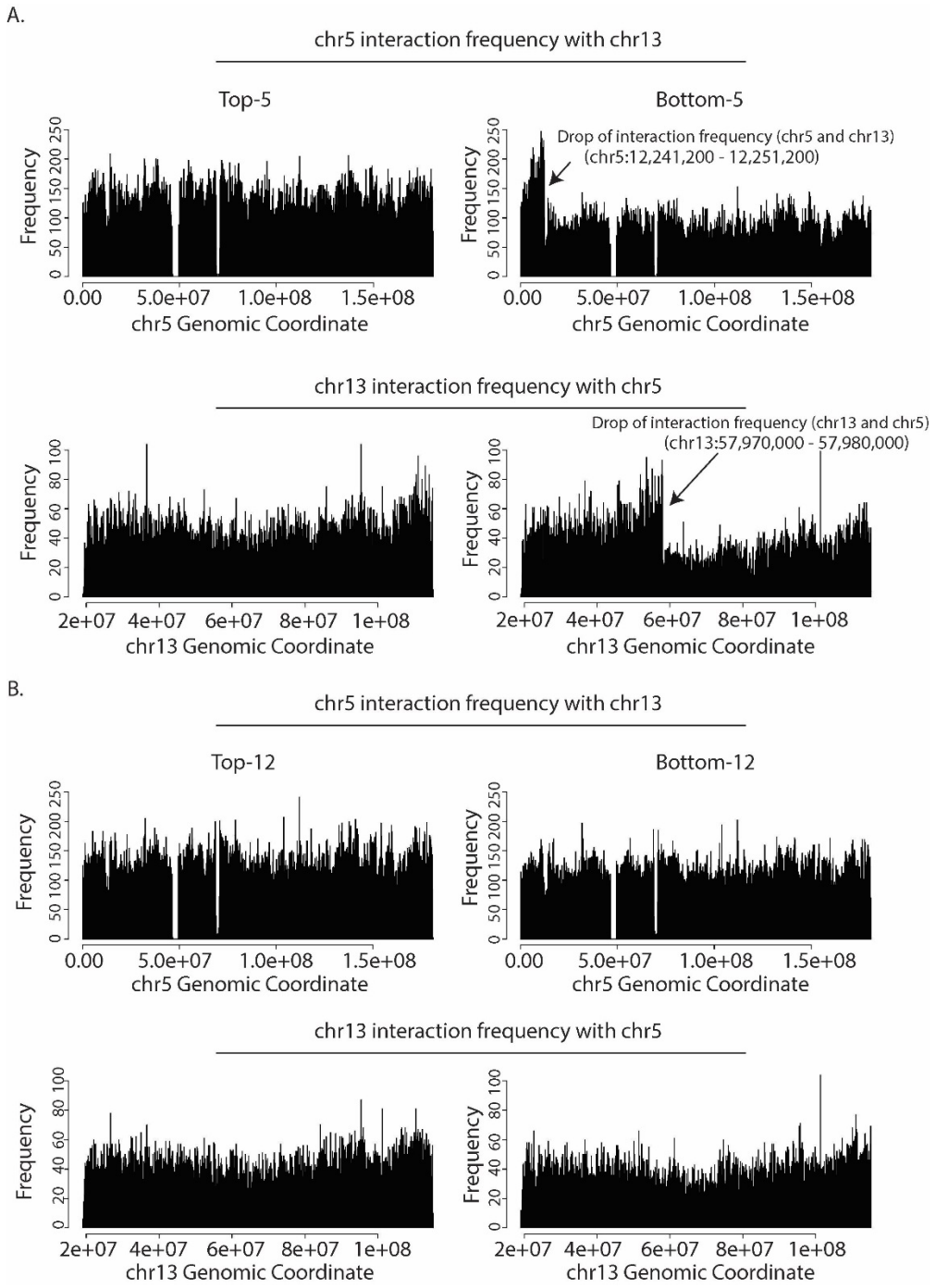

Supplementary Figure 6. Translocation between chr5 and chr13 is specific to migration through 5µm constrictions. (A) Top panel: Contact frequency of chr5 genomic coordinates with chr13 in Top-5 cells (left) and Bottom-5 cells (right). Bottom panel: Contact frequency of chr13 genomic coordinates with chr5 in Top-5 cells (left) and Bottom-5 cells (right). Black arrows indicate a decrease in contact frequency between chr5 and chr13 (Top panel) and chr13 and chr5 (Bottom panel) indicating the end of the translocated region. (B) Top panel: Contact frequency of chr5 genomic coordinates with chr13 in Top-12 cells (left) and Bottom-12 cells (right). Bottom panel: Contact frequency of chr13 genomic coordinates with chr5 in Top-12 cells (left) and Bottom-12 cells (right). A drop in contact interaction frequency is not observed due to undetectable t(5,13).

Since A375 cells have an average of 3 copies of each chromosome per cell, this can be extrapolated to this translocation occurring on one chromosome copy in ~18% of the Bottom-5 cells and 9% of the Bottom20-5 cells (Figure 6C). Interestingly, this translocation was not detected in the cells that did not undergo constricted migration (Top-12, Top-5, Top20-5 and Bottom-12) as the fraction of reads coming from the translocation site matched the random background level of interchromosomal interactions in the Hi-C contact map (Figure 6C, negative control). The absence of this translocation in non-migratory cells (Top-12, Top-5 and Top20-5) and in Bottom-12 cells suggests that the translocation event may arise due to the physical stress on the nucleus during constricted migration. However, it is also possible that this translocation was present at undetectable levels in the heterogeneous control A375 population, and we are selecting the cells with this translocation during sequential migration.

In addition to translocations, changes in chromosome copy number have been previously reported after constricted migration (Irianto et al., 2017a). We therefore followed a published approach (Servant et al., 2018) to use raw read counts from our Hi-C data to investigate possible copy number variations (CNV) due to constricted migration in A375 subpopulation of cells (Figure 6D). The control population of A375 cells already exhibits non-uniform copy number across chromosomes and chromosome regions (Figure 6D, top panel). When comparing the subpopulations of A375, most of the chromosomes maintained their copy numbers independent of constricted migration. However, cells that have undergone constricted migration (Bottom-5 and Bottom20-5) exhibit notable copy number loss in chr13 (Figure 6D, bottom panel).

Beyond revealing translocations, interchromosomal contact data can reveal changes in patterns of whole chromosome territory interactions between conditions. So, we next sought to explore how the interchromosomal fraction (ICF) of interactions (Heinz et al., 2018) across the genome varies among the cells that have undergone constricted migration (Figure 6E). Interestingly, we observe a decrease in ICF of chr13 (Figure 6E, top panel, indicated by black arrow) in Bottom-5 cells. This is not likely to be explained purely by copy number loss at chr13, as this would decrease both inter and intra-chromosomal contacts rather than changing the ratio between the two. Additionally, smaller chromosomes (chr14-chr22) display an overall increase in ICF in Bottom-5 cells (Figure 6E, top panel, indicated by black box) but a decrease of ICF in Bottom-12 cells (Figure 6E, bottom panel, indicated by black box). This measurement could indicate that smaller chromosomes differ in their relative compactness and intermixing depending on constricted migration.

Cells that have undergone constricted migration exhibit metastatic phenotypes in 3D models

To investigate whether the cells that had undergone multiple rounds of constricted migration show metastatic behavior in more biologically-relevant environments, we embedded all A375 subpopulations in 3D collagen gel matrices as described previously (Denais et al., 2016). Bottom-5 and Bottom20-5 cells embedded in collagen with a density of 2.42 mg/mL, displayed long cytoplasmic protrusions and large nuclear deformations (Figure 7A, right panel and Figure S7) 4 days after seeding, suggesting that the cells are attempting to migrate through the collagen pores. In contrast, cells that did not undergo constricted migration in the Transwell (Top-12, Top-5, Top20-5 and Bottom-12) did not exhibit cellular or nuclear shape changes but rather round nuclei,

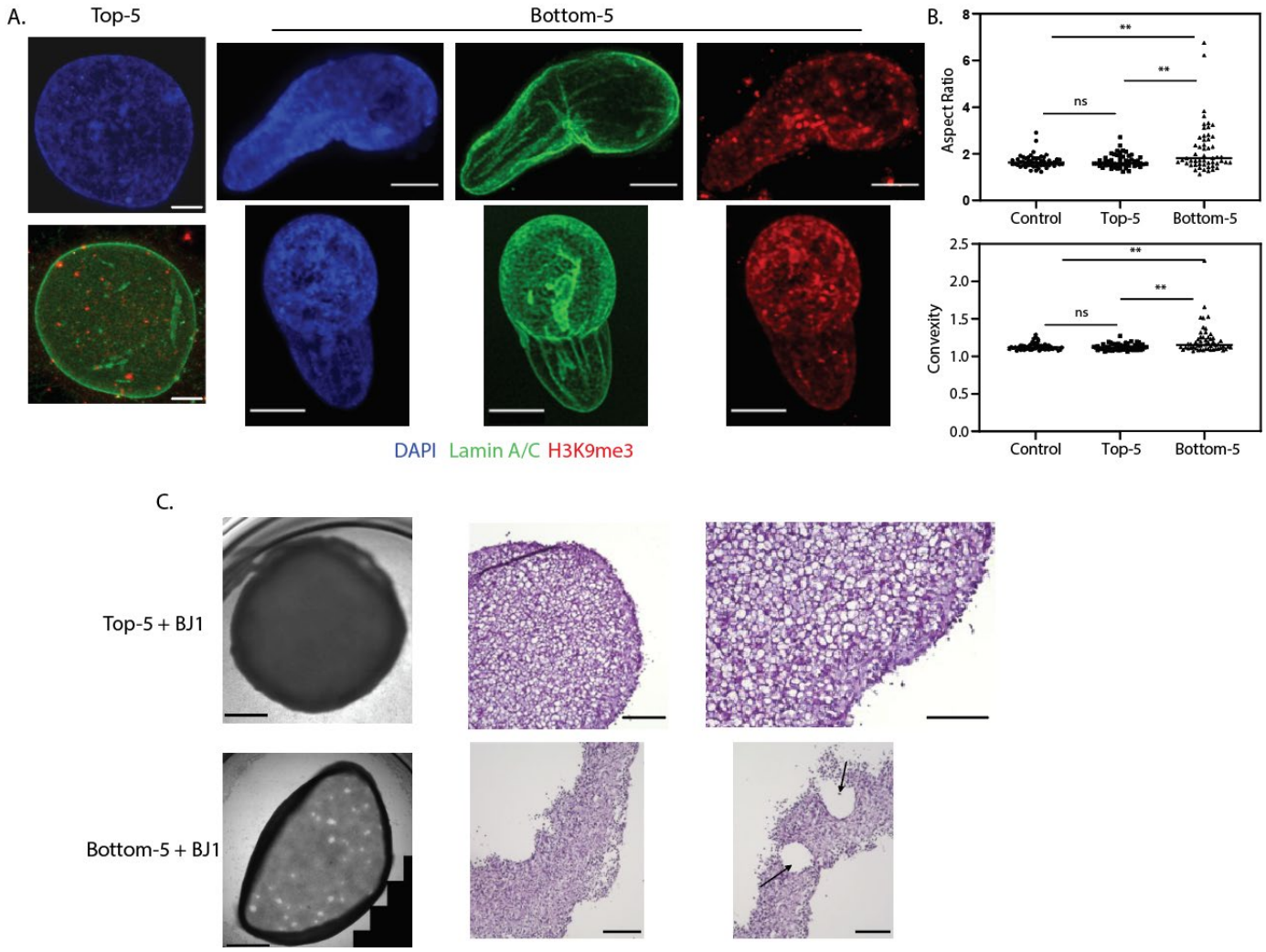

Figure 7. 3D models reveal metastatic phenotypes of cells that have undergone constricted migration. (A) A375 cells embedded on 3D collagen matrices show differences in their nuclear appearance. Nuclei of Top-5 (left panel) and Bottom-5 cells (right panel) stained for DAPI (blue), Lamin A/C (green) and H3K9me3 (red). Scale bars (white) indicate a length of 5 µm. For 3D reconstruction visualization, see Movie S5 and S6. (B) Measurements of nucleus aspect ratio (major axis/minor axis) in Control (n = 54), Top-5 (n = 52) and Bottom-5 (n = 53) (Top graph). Top-5 vs Control (p = 0.8232); Bottom-5 vs Top-5 (**p = 0.0054); Bottom-5 vs Control (**p = 0.0031) as calculated by two-tailed t-test. Measurements of nucleus convexity (convex volume/volume) in Control (n = 54), Top-5 (n = 52) and Bottom-5 (n = 53) cells (Bottom graph). Top-5 vs Control (p = 0.4621); Bottom-5 vs Top-5 (**p = 0.001); Bottom-5 vs Control (**p = 0.0067) as calculated by two-tailed t-test. (C) Free floating organoids of A375 cells exposed to 5-µm transwell co-cultured with BJ-1 cells as captured by phase contrast microscopy after 24 hours (left panel). Scale bars (black) indicate a length of 3.5mm. H&E stained section of Top-5 and Bottom-5 organoids. Scale bars indicate a length of 200 µm. Arrows in bottom panel indicate holes characteristically seen in Bottom-5 organoids.

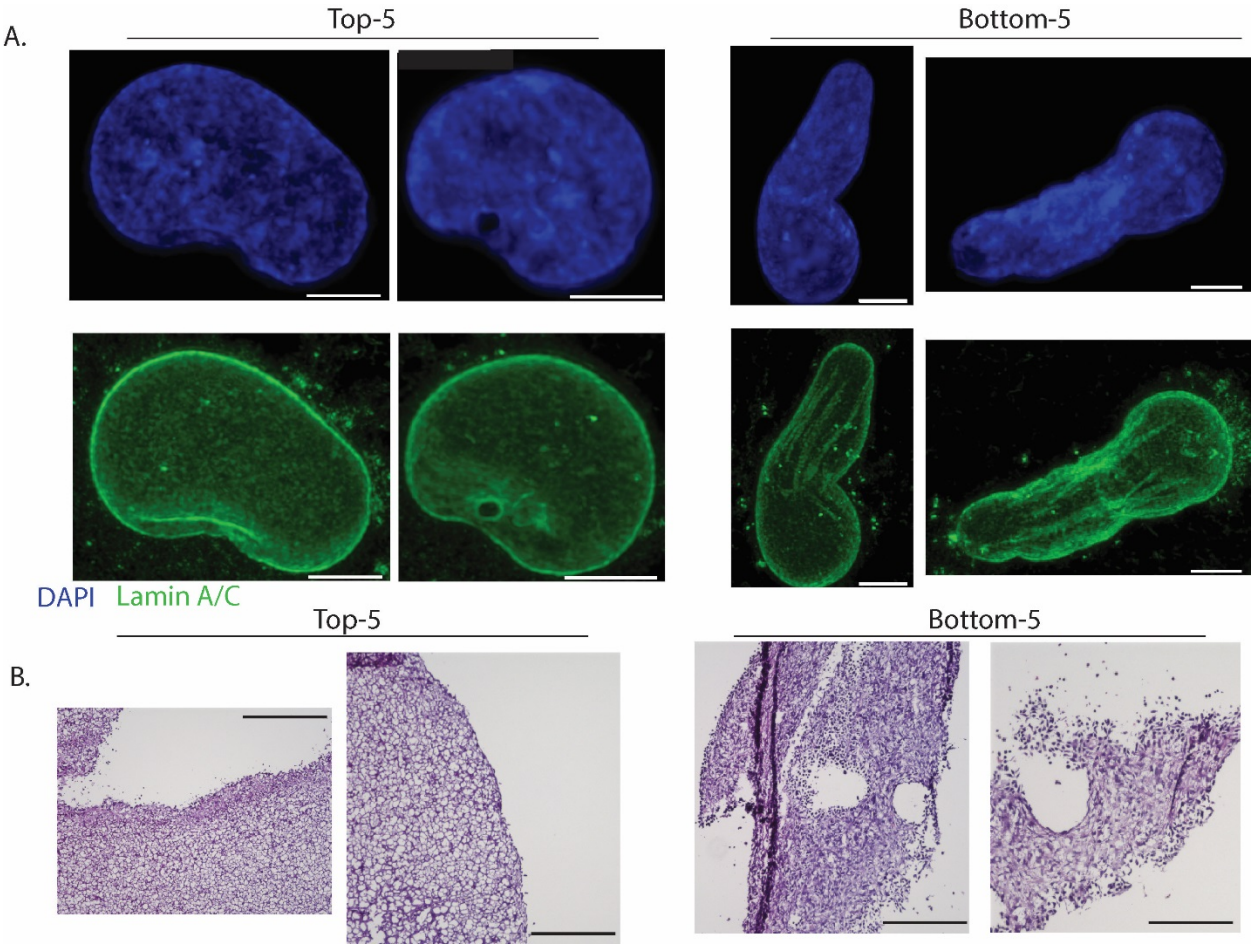

Supplementary Figure 7. 3D models reveal metastatic phenotypes of cells that have undergone constricted migration. (A) Max projection confocal images of Top-5 (left panel) and Bottom-5 (right panel) nuclei visualizing DAPI (blue) and Lamin A/C (green). Scale bars (white) indicate a length of 5 µm. (B) H&E staining of 3D co-cultured organoids derived from Top-5 (left panel) and Bottom-5 (right panel). Scale bars (black) indicate a length of 200 µm.

suggesting an inability of these cells to move through the pores created by the collagen fibers (Figure 7A, left panel and Figure S7, Movie S5 and S6). Quantification of nuclear shape differences between these subpopulations of cells by measuring the roundness of the nucleus (Figure 7A*ii*) clearly distinguished cells that had undergone constricted migration from cells that did not, indicating that the ability to deform their nucleus in a 3D environment is a key distinguishing factor among the A375 subpopulation of cells.

With the emerging applications of organoid systems in bridging basic cancer research to pre-clinical models (Xu et al., 2018), we took advantage of this system to investigate whether we observe any differences in organoid formation and interaction with healthy stromal cells between non-migratory and highly migratory melanoma cells. We co-cultured each A375 subpopulations of cells with normal human foreskin fibroblasts (BJ-1) on a low adherent surface to induce aggregation and attachment of cells to each other. While this system has been widely used to

investigate interactions between mesenchymal stem cells and other cells of choice (San Martin et al., 2017, Kim et al., 2014, Takebe and Wells, 2019) this is, to our knowledge, the first use of a free floating epithelial-stromal organoid to model melanoma.

When mixed with healthy skin fibroblasts, Control and Top-5 cells formed a round free-floating organoid structure. Hematoxylin and eosin (H&E) staining of sections of this organoid revealed an epithelial-like layer of cells around the outer-edge of the organoid (A375 cells) and an inner stromal mass likely composed of BJ-1 cells (Figure 7B*i*). Top-5 cells displayed a tight arrangement of epithelium in the outer compartment and an even distribution of BJ-1 in the inner compartment (Figure 7B*i*, right panel). In contrast, when mixing the highly migratory cells (Bottom-5 and Bottom20-5) with fibroblasts, we observed the slower formation of a looser, porous and non-compartmentalized organoid (Figure 7B*ii*). H&E staining of these organoids revealed disorganized aggregations of epithelium clusters in the outside of the organoid, which likely stems from the decreased cell-cell attachments and highly migratory phenotypes of these migratory cells shown above (Figure 1). Additionally, in the organoids formed by the highly migratory melanoma cells, we observe channel-like openings in the stromal compartment that are reminiscent of vasculogenic mimicry as previously reported in different tumors including melanoma (Spiliopoulos et al., 2015, Kim et al., 2019). These results demonstrate that cells that have undergone sequential confined migration in an artificial Transwell system display biologically relevant aggressive cancer-like phenotypes in their interactions with other healthy cells.

Discussion

Constricted migration is an important phenomenon in cancer metastasis and presents a major challenge to nuclear mechanics. Major avenues of previous research have separately investigated the role of the nucleus in confined migration, the impact of migration on linear DNA integrity, and the role of 3D genome structure in cancer. Our present results bridge these fields, revealing changes in spatial chromosome compartmentalization specific to cells that have passed through numerous constrictions smaller than their nucleus. These genome structure changes are associated with a notable change in cell and nucleus phenotypes whether the cells are migrating on a 2D surface, squeezing through a collagen matrix, or aggregating in organoids. Cells proficient at confined migration more often deform their nuclei, elongate their cell body, and have fewer cell-cell attachments.

A major question raised by our results is whether the differences in 3D genome structure we see in cells that have undergone confined migration (Bottom-5 and Bottom20-5) result from a selection process on an initially heterogeneous population or a “training process” where confined migration itself causes chromosome structure changes. We first note that trying to determine “selection or training” is in many ways a false dichotomy. It is very plausible that cells which are initially primed for confined migration in a heterogeneous tumor begin to squeeze through tight junctions, and that then their chromosome structure is further rearranged as a result of the nucleus deformations. Overall, our data provide evidence consistent with the idea that both processes are taking place.

First, our isolation of A375 cells that cannot migrate at all, even given 10 chances to go through a wide pore (Top-12 cells), is a clear demonstration that the initial A375 population is

heterogeneous. These cells have been previously shown to display heterogeneity in their metastatic capacity (Kozlowski et al., 1984) and overall within melanoma lesions, a select group of cells can gain the ability to metastasize, and that further diversification and phenotype change can occur as a result of metastasis (Damsky et al., 2010). The genome structures and gene expression patterns specific to this subset informs us about the properties of cells that cannot migrate. On the other hand, the fact that our Bottom-12 cells, which have passed through a large pore, present with genome structure differences compared to Bottom-5 cells shows that we are not simply distinguishing between cells with a pre-existing ability to migrate. There are cellular, nuclear, and genome organization properties specific to confined migration. Further, some structures and phenotypes of Bottom-5 cells, such as the new chromosome 5-13 translocation and extremely elongated cell shapes, are not detectable in the original control population. This suggests that confined migration itself can induce some of the changes we observe. As passage through a constriction physically moves the chromosomal regions in the nucleus, certain interactions, such as the strongest B-B interactions in our data, may be pulled apart as suggested by chromatin stretching previously described (Irianto et al., 2017b) and loss of B-B interaction strength with confined migration observed in neutrophils (Jacobson et al., 2018). Meanwhile, loci previously more distant are given an opportunity to associate and may form new aggregates through phase separation. This may be an explanation for the strengthening of interactions we observe between previously weak B compartments and stronger B compartment regions. Future work, such as sequential migration of individual clones, single cell Hi-C, and approaches to monitor individual cells' chromosome folding through rounds of constriction, will help further identify which genome structures pre-exist and favor migration and which are newly caused by the stresses of migration.

Our results suggest that the confined migration-specific 3D genome structure serves several potential biological purposes. First, we observe an overall correlation between spatial compartmentalization changes and gene expression alterations, and the altered genes relate to migratory ability. For example, in Bottom-5 cells, we observe downregulation of a group of genes important for cell-cell/matrix adhesion (CADM3, CADM1, ITGA9). Why would 3D genome changes be needed to accompany gene expression changes? Altered local gene regulation alone can be sufficient to explain temporary changes in cellular behaviors in response to a stress or stimulus, and these changes do not require 3D genome rearrangement (Jin et al., 2013). But our data suggests that migration behaviors of the different A375 sub-populations are stably divergent. From our observations, we propose that the stability of this phenotype is encoded in the 3D genome structure change we measure, since moving whole genomic regions to different spatial and chromatin environments is less reversible than transiently regulating individual genes. Further, since these differences persist through several passages in culture, this raises the possibility that 3D genome changes after confined migration could underlie the distinct phenotype and increased *in vitro* invasiveness of cancer cells derived from metastatic sites compared to those from primary tumors or normal tissue (Oppenheimer, 2006). We propose that the different behavior of our cell subpopulations in organoid cultures with normal fibroblasts is inherent to changes in their genome structures which are, in turn, physiologically relevant to phenomena in cancer progression.

Beyond gene regulation, our results suggest a role for chromosome structure change in modulating the physical properties of the cancer cell nucleus. Our results show that the nuclei of Bottom-5 cells deform more than Top-5 cells when embedded in a collagen matrix or even when spontaneously migrating on a 2D surface. Previous research has shown that nucleus stiffness can be altered by increasing or decreasing the overall expression of Lamin A/C or by changing overall levels of heterochromatin (Lammerding et al., 2006, Davidson et al., 2014, Stephens et al., 2017, Stephens et al., 2018). But, the apparent change in nucleus pliability observed in the current study cannot be explained by changes in overall Lamin A/C content or heterochromatin levels: Lamin A/C and H3K9me3 levels were constant as measured by both immunostaining and western blot. Instead, we observed a redistribution of Lamin A/C and H3K9me3 localization in the nucleus, with individual heterochromatin foci originally in the interior of the nucleus merging at the periphery and Lamin A/C becoming less evenly distributed. Our observations suggest that changing levels of Lamin A/C and heterochromatin are not always required to increase constricted migration potential and that re-localization of these proteins and chromosome regions can be important to provide a rigid enough nucleus to withstand physical deformations but also soft enough to be able to successfully undergo constricted migration. Future work will be required to determine how the 3D genome changes we observe translate into quantitative differences in nucleus physical properties.

The altered heterochromatin localization we observe by imaging translates to, and is more deeply characterized by, the alterations in chromosome compartmentalization we observe with Hi-C. The observation that regions which increase their B compartment interactions also gain more distal interactions is consistent with our imaging observation that disparate heterochromatin foci come together at the nuclear periphery in confined migrating cells. Interestingly, many of the regions with altered compartmentalization do not show a connection to gene regulation. In fact, we observe a striking enrichment of regions with no genes at all among the set of regions that switch from the A to the B compartment in confined migration. This suggests that the genome structure changes we observe have a role beyond gene regulation, and we hypothesize that these switches are primarily involved in changing physical properties of the chromosome structure and therefore nucleus adaptability to constriction.

Our data also provide insight into some basic questions about 3D genome organization principles. As described above, our data allow conceptual links between changes in contacts observed in Hi-C data and the appearance and localization of chromatin types observed by imaging. Further, our observation that compartments, compartment strength, and whole chromosome interactions change while TADs are unaltered reinforces the idea that these are separate and largely independent layers of genome organization (Mirny et al., 2019, Schwarzer et al., 2017). These changes also suggest that the compartment and whole chromosome level of genome structure are more important in nucleus physics and deformation than is the TAD and loop level of organization. Meanwhile, our observation that local punctate interactions change around sites where gene expression changes echo previous evidence that collisions between loop extrusion and transcription can influence local contact patterns (Brandao et al., 2019).

Are the 3D genome changes we observe in our constricted migration cell population diagnostic of metastatic potential? Previous reports have sometimes detected gene expression signatures in

primary tumors that may be predictive of metastasis(Ramaswamy et al., 2003). Nuclear morphology abnormalities ("nuclear atypia") are also already used clinically as a marker of cancer aggressiveness (Kadota et al., 2012). Recent reports have taken advantage of microfluidic engineering to predict metastatic potential of breast cancer cells based on their morphological features (Yankaskas et al., 2019). But, beyond being a marker, the biological significance of such abnormalities and what chromosome structure changes accompany them have not been defined. Here, we provide evidence that chromosome structure changes could link metastatic gene expression signatures with the abnormal nuclear appearance of aggressive cancer. Our results reveal chromosome spatial compartmentalization changes in genomic regions related to metastatic potential in a highly invasive subset of A375 cells. Future work will be needed to investigate whether such changes are also observed in patient metastatic melanoma samples. Our data provides a foundation for future investigation of whether similar structural changes occur after constricted migration in other cancer types and therefore constitute 3D genome structure signatures of metastatic cancer potential.

Acknowledgements

We thank Mariano Labrador, Jacob Sanders, and Yang Xu for insightful discussion. We thank Jan Lammerding for advice about the project. We thank Bas van Steensel for providing the LAD type annotations. BJ1-hTERT cells were provided by Adayabalam Balajee at Oak Ridge Institute of Science and Education. Confocal images were obtained at the University of Tennessee Advanced Microscopy Imaging Core. This research was supported in part by a Ralph E. Powe Junior Faculty Enhancement Award from Oak Ridge Associated Universities to R.P.M. and by NIH NIGMS grant R35GM133557 to R.P.M. R.G. is supported in part by a Yates Dissertation Fellowship from UTK. D.T. was supported in part by a UTK Summer Undergraduate Research Internship award.

Author Contributions

R.G. and R.P.M. conceived the project, designed the experiments and wrote the paper with input from all authors. R.G. performed genomic, cell culture, and imaging experiments and bioinformatics data analysis. R.SM. advised on project and organoid design and performed 3D organoid experiments and histology. P.D. assisted with computational analysis. T.I.R. performed 3D collagen experiments and quantification. D.T provided experimental assistance in histology and performed single cell migration video analysis. T.F. performed part of the sequential migration assays and Hi-C.

Declaration of Interests

All authors declare no competing interests.

Supplementary Tables

Sample	Total Raw Reads	Both Sides Mapped	Valid Pairs	Unique Valid Pairs	% Cis Interactions	% Dangling Ends
Control-R1	201,352,157	124,670,760	123,653,686	107,358,325	61.2	0.35
Control-R2	200,881,087	102,710,892	101,397,252	80,394,938	47.7	0.31
Top10-R1	320,786,521	163,004,931	161,788,811	132,650,834	55.6	0.23
Bottom10-R1	386,733,576	193,207,211	191,853,175	152,440,505	60.3	0.21
Top10-R2	164,616,353	84,226,628	83,087,615	68,000,595	48.7	0.28
Bottom10-R2	107,320,517	54,380,776	53,662,580	43,911,557	49.2	0.45
Top20-R1	142,531,635	66,090,879	62,567,577	49,317,732	47.7	0.60
Bottom20-R1	159,577,275	73,992,021	70,695,806	57,329,882	49.7	0.44
Top12-R1	117,695,787	90,932,905	90,442,670	81,815,020	43.0	0.39
Bottom12-R1	110,637,334	85,346,366	84,975,979	76,728,534	37.0	0.30
Top12-R2	145,063,083	110,772,496	110,380,318	98,396,558	40.4	0.26
Bottom12-R2	126,055,079	96,662,104	96,161,324	86,277,860	43.5	0.34

Table S1. Summary Statistics for Hi-C Sequencing Experiments, Related to STAR Methods.

Sample	Total Reads after rRNA removal	Mapped Reads	Percent Mapped Reads
Control-R1	25,802,932	23,454,526	90.9
Control-R2	44,936,964	39,168,478	87.16
Top5-R1	57,420,692	49,189,316	85.66
Top5-R2	40,240,820	34,943,927	86.84
Bottom5-R1	44,784,816	37,982,597	84.81
Bottom5-R2	42,149,066	36,445,763	86.47
Top20-5-R1	39,235,465	36,102,375	92.01
Top20-5-R2	97,958,087	89,841,371	91.71
Bottom20-5-R1	107,282,198	98,413,826	91.73
Bottom20-5-R2	54,332,623	49,381,035	90.89
Top12-R1	47,231,386	42,228,487	89.41
Top12-R2	44,863,196	41,601,169	92.73
Bottom12-R1	43,203,103	38,744,667	89.68
Bottom12-R2	8,436,059	7,655,956	90.75

Table S2. Summary Statistics for RNA Sequencing Experiments, Related to STAR Methods.

Supplementary Movie Captions

Supplementary Movie 1. Phase contrast live cell imaging in a 2D culture dish of a Top-5 cell. This cell is exhibiting amoeboid like migration.

Supplementary Movie 2. Phase contrast live cell imaging in a 2D culture dish of Bottom-5 cells. An integration of amoeboid and lobopodian/lamellipodia type of migration is observed.

Supplementary Movie 3. 3D rendering of Top-5 nucleus using Leica Sp8 software displaying Lamin A/C (green) and H3K9me3 (red)**.** Scale bars (white) indicate a length of 2 μm.

Supplementary Movie 4. 3D rendering of Bottom-5 nucleus using Leica Sp8 software displaying Lamin A/C (green) and H3K9me3 (red)**.** Scale bars (white) indicate a length of 2 μm.

Supplementary Movie 5. 3D rendering of nucleus of collagen embedded Top-5 cell stained with DAPI (blue) displays a uniform distribution of Lamin A/C (green). Scale bars (white) indicate a length of 2 μm.

Supplementary Movie 6. 3D rendering of nucleus of collagen embedded Bottom-5 cell stained with DAPI (blue) displays an elongated shape and an altered distribution of Lamin A/C (green) with appearance of fiber like structures on the side of the constriction. Scale bars (white) indicate a length of 5 μm.

STAR METHODS

KEY RESOURCES TABLE

REAGENT or RESOURCE	SOURCE	IDENTIFIER
Antibodies (IF)		
Lamin A/C	Santa Cruz	sc-376248
Lamin B1	Abcam	ab133741
H3K9me3	Abcam	ab176916
Alexa Fluor 594	Invitrogen	R37117
Alexa Fluor 488	Invitrogen	R37120
Antibodies (Western Blot)		
Beta Actin – Rabbit Polyclonal	Thermo Fisher	PA1-16889
Beta Actin – Mouse Monoclonal	Thermo Fisher	MA1-140
Goat anti-rabbit secondary	Licor	92568071
Goat anti-mouse secondary	Licor	95-32210
Chemicals		
DMEM	Corning	10-013-CV
FBS	Corning	35-010-CV
Pen-Strep	Gibco	14140-122
L-Glutamine	Gibco	25030-081
Medium 199	Lonza	12-119F
Hygromycin B	Corning	30-240-CR
Trypsin	Corning	25053CI
RIPA buffer	Thermo Scientific	I89900
Collagen	Corning	354236
protease inhibitors/EDTA	GenDepot	50-101-5485
phosphatase inhibitors	GenDepot	50-101-5488
micrococcal nuclease	Thermo Scientific	FEREN0181
BCA Protein Assay Kit	Thermo	234225
4-12% Bis-Tris Plus gels	Invitrogen	NW04120BOX
PVDF membranes	Invitrogen	B1000
O.T.C	Sakura	4583
Critical Commercial Assays		
RNA easy Kit	Qiagen	74134
rRNA Depletion Kit	New England Biolabs	E63105
Ultra II RNA library prep kit	New England Biolabs	E7770G
Multiplex Oligos for Illumina	New England Biolabs	E7335G

Rapid Chrome Kit	Thermo Fisher	9990001
Deposited Data		
Hi-C, RNA-Seq and ATAC-Seq from A375 cell line	This study	GEO:XXXXXXXXX
Experimental Models: Cell Lines		
A375	ATCC	CRL-1619
BJ1-hTERT	Clontech	CCD00309196
Transwell Migration Experiments		
Fibronectin	Corning	354008
Transwell Filters (12µm)	VWR	10769-224
Transwell Filters (5µm)	VWR	10769-236
Software and Algorithms		
Bowtie2	(Langmead and Salzberg, 2012)	http://bowtie-bio.sourceforge.net/bowtie2/index.shtml
C-World	Job Dekker Lab	https://github.com/dekkerlab/cworld-dekker
STAR	(Dobin et al., 2013)	https://github.com/alexdobin/STAR
MACS2	(Zhang et al., 2008)	https://github.com/taoliu/MACS
HTSeq	(Anders et al., 2015)	https://htseq.readthedocs.io/
DESeq2	(Love et al., 2014)	https://bioconductor.org/packages/release/bioc/html/DESEQ2.html
Bedtools	(Quinlan and Hall, 2010)	http://bedtools.readthedocs.io/en/latest/
Samtools	(Li et al., 2009)	http://samtools.sourceforge.net/
BBTools		https://github.com/kbaseapps/BBTools
CNV estimation	(Servant et al., 2018)	https://github.com/nservant/cancer-hic-norm

CONTACT FOR REAGENT AND RESOURCE SHARING

Further information and requests for resources and reagents should be directed to and will be fulfilled by the Lead Contact, Rachel Patton McCord (rmccord@utk.edu).

EXPERIMENTAL MODEL AND SUBJECT DETAILS

Cell Lines and Cell Culture

A375 human melanoma cells were obtained from ATCC (CRL-1619). Cells were grown using complete DMEM medium (Corning – 10-013-CV; 10% FBS, 1% Pen-Strep, 1% L-Glutamine) at 37ºC supplied with 5% CO_2.

BJ1-hTERT cells used for 3D organoid co-culture were grown in a 4:1 mixture of DMEM (containing 4mM L-glutamine, 4.5g/L glucose 1.5g/L sodium bicarbonate) and Medium 199. Base media was supplemented with 0.01 mg/mL hygromycin B and 10% FBS.

METHOD DETAILS

Sequential Transwell Migration

For the sequential transwell migration, we used transwells with 12 µm (VWR-10769-224) and 5 µm pore sizes (VWR-10769-236). Briefly, the bottom of the transwells were coated with 40 µL of 10 µg/mL fibronectin for ~ 45 minutes. 24 well plates were prepared for transwell migration assay adding 500 µL of 1x DMEM (Corning) with full supplements per well. A375 cells were detached from culture dishes at 80-90% confluency and aliquoted to 100,000 cells per 100 µL of 1xDMEM. Each transwell was placed into its corresponding well of the 24 well plate and 100 µL of the cell suspension was added to the top of each filter. Cells were incubated at 37ºC, 5% CO_2 and allowed to migrate for 24 hours. After the 24-hour incubation, migration efficiency was quantified as follows. First, freely floating cells were removed from the top of the filter (unmigrated; "Top" cells) and from the well beneath the filter (migrated "Bottom" cells) and placed in two separate tubes. Then, 400 µL of trypsin was added into the bottom chamber of the 24 well plate and 200 µL of trypsin was added into the top chamber to detach any remaining attached cells. Recovered cells after trypsinization were added to the unmigrated or migrated tubes, accordingly. Cells were spun down (1000 rpm, 5min) and counted (using trypan blue) to calculate % migration such as: #bottom/(#top+#bottom). Additionally, a small aliquot of cells was saved for immunofluorescence (IF). The rest of the cells were seeded into wells of a 24-well plate to expand. When cells reached 80-90% confluency, another transwell migration was performed (R2). A375 Top and Bottom cells were detached and counted. Two transwell filters were prepared as previously described (one for Top and one for Bottom). Then 100,000 cells suspended in 100 µL of 1xDMEM without supplements were seeded into the transwell filters. After 24-hour incubation at 37ºC and 5% CO_2, cells were trypsinized as previously described to quantify migration efficiency. Only the cells that were always on top (Top of Top) and the cells that were always on the bottom (Bottom of Bottom) were saved and grown for further sequential rounds of migration. This process was repeated for 10 and 20 rounds of migration which lead to the generation of A375-5-NM10, A375-5-M10, A375-12-NM10, A375-12-M10, A375-5-NM20 and A375-5-M20.

2D Single Cell migration

Live cell imaging

To track single cell movement in 2D, A375-C, A375-NM and A375-M cells were seeded on wells of a 6-well plate at a 30,000 cells/well density. After cells were attached, live cell imaging was performed using the EVOS FL Auto microscope at 40X magnification. Images were acquired every 10 minutes for a 24-hour time period.

Cell morphology analysis

Parameters that describe cell morphology such as solidity and aspect ratio were quantified using the Shape Descriptors plugin in ImageJ.

Immunocytochemistry

IF staining

Approximately 50,000 – 100,000 cells for each sub-population of A375 were seeded into either poly-D-lysine treated coverslips or 35-mm coverslip bottom dishes. Cells were allowed to attach overnight and then crosslinked with 4% formaldehyde for 10 min followed by three, 5-minute washes with PBS. After washing, cells were permeabilized with permeabilization buffer (10% goat serum, 0.5% Triton in PBS) for 1 hour at room temperature. After the incubation, primary antibodies (Lamin A – sc-376248, Lamin B1 – ab133741, H3K9me3 – ab176916), diluted in antibody dilution buffer (5% Goat serum, 0.25% Triton in PBS) were added and incubated overnight at 4°C. After primary antibody incubation, cells were washed 3 times with PBS for 5 minutes for each wash. Cells were then incubated with secondary antibodies (Alexa Fluor 594 and Alexa Fluor 488) per manufacturer's directions (2 drops of secondary antibody/1mL of PBS – R37117 and R37120) for 30 minutes at room temperature. After secondary antibody incubation, cells were washed 3 times with PBS and sealed using mounting media with DAPI. Slides were treated in the mounting media for 24 hours before imaging.

Cells were imaged using a Leica Sp8 Confocal microscope was equipped with a 63x oil immersion objective.

Nuclear morphology analysis

To analyze the area, perimeter, solidity and aspect ratio of nuclei, Image J plugins were used (Area, Perimeter and Shape Descriptors). Lamin A/C and H3K9me3 radial distribution was quantified using Measure Object Intensity Distribution module in Cell Profiler. Mean fractional intensities for each bin specified (4 total bins; starting from innermost (bin1) to outermost (bin4) radial position) was plotted.

Western Blot

A375 cells were trypsinized as previously described, and approximately 5 million cells were collected by centrifugation (1000 rcf, 5 min, room temperature). The cell pellets were resuspended in 300 ml of RIPA buffer (Thermo Scientific, I89900), supplemented with protease inhibitors/EDTA (GenDepot 50-101-5485), and phosphatase inhibitors (GenDepot 50-101-5488). Cells were then incubated on ice for 10 minutes. DNA was degraded by adding 6 µl of micrococcal nuclease (0.5 U/ml stock, Thermo Scientific, FEREN0181) and 12 µl of calcium chloride (100 mM stock) to each lysate, followed by incubation at 37°C for 15 min. Nuclease activity was inhibited by subsequent incubations at 68 °C for 15 min, and ice for 10 min. Protein samples were stored at −80 °C until use. Protein concentration was measured using the BCA Protein Assay Kit. Thermo (234225), according to the manufacturer's instructions.

Denatured protein samples were resolved using a mini gel tank (Invitrogen, A25977) for 35 min at 200V, using 4-12% Bis-Tris Plus gels (Invitrogen, NW04120BOX) for all targets. Protein was transferred to low fluorescence PVDF membranes using the mini Bolt Blotting System

(Invitrogen, B1000), along with system-specific reagents. Blotting was performed using the Odyssey TBS blocking system (Licor, 927-400000), according to the manufacturer's protocol. Briefly, membranes were activated with methanol after transfer (1 min, RT), washed twice with milliQ water (5 min), twice with TBS (2 min), and blocked with Odyssey TBS blocking solution for 1 hour at RT. Primary antibodies were diluted in blocking buffer (containing 0.2% Tween), and incubated over night at 4°C as follows: H3K9me3 (1:1000, ab176916), LaminA/C (1:1000, sc-376248) and LaminB1 (1:1000, ab133741). Beta actin was used as a loading control, using the appropriate antibody (1:10,000; rabbit polyclonal PA1-16889, Thermo Fisher or 1:10,000; mouse monoclonal MA1-140, Thermo Fisher) alongside with the targets of interest. Detection was carried out using the following secondary antibodies: goat anti-rabbit (1:10,000; IRDye 680RD [92568071]; Licor) and goat anti-mouse (1:10,000, IRDye 800CW [95-32210]; Licor). Secondary antibodies were diluted in Odyssey TBS blocking buffer containing 0.2% Tween and 0.01% SDS. Membranes were incubated in secondary antibody for 1 hour at RT, followed by three washes (TBST, 5 min each).

Images of near infrared fluorescent signal were acquired using an Odyssey scanner (Licor) in both the red and green channels. Signal was quantified using the Image Studio software (Licor).

Hi-C

Library Preparation

Hi-C libraries were prepared for each cell sub-population (A375-C, A375-NM10, A375-M10, A375-NM20, A375-M20, A375-12-NM and A375-12-M) as previously described (Golloshi et al., 2018) including two biological duplicates for each condition. Briefly, 10 million cells were grown in T-75 cell culture flasks to 80-90% confluency and crosslinked with 1% formaldehyde for 10 min. Crosslinked cells were then suspended in lysis buffer to permeabilize the cell membrane and were dounce homogenized. Chromatin was then digested in-nucleus overnight using DpnII restriction enzyme. Digested ends were filled in with biotin-dATP, and the blunt ends of interacting fragments were ligated together. DNA was then purified by phenol-chloroform extraction. For library preparation, the NEBNext Ultra II DNA Library prep kit (NEB) was used for libraries with size ranges from 200-400bp. End Prep, Adaptor Ligation, and PCR amplification reactions were carried out on bead bound DNA libraries.

Sequencing was performed at the Oklahoma Medical Research Foundation Clinical Genomics facility using the Illumina HiSeq 3000 platform with 75 bp paired end reads or a NovaSeq 6000 with 50 bp paired end reads. Sequencing reads were mapped to the human genome (hg19), filtered, and iteratively corrected as previously described (Imakaev et al., 2012) (https://github.com/dekkerlab/cMapping). All Hi-C contact matrices were scaled to a sum of 1 million interactions to allow comparisons between conditions in downstream analysis. For library quality and mapping statistics see Table S1.

Compartment Analysis

Compartment analysis was performed by running principal component analysis using matrix2compartment.pl script in the cworld-dekker pipeline available on GitHub (https://github.com/dekkerlab/cworld-dekker). The PC1 value was then used to determine

compartment identity for 100 and 250Kb binned matrices. We considered PC1 values greater than 0.01 to be A compartment and less than -0.01 to be B compartment for this analysis and determination of compartment switches.

Saddle Plots

Saddle plots were constructed to investigate changes in interaction frequency between or within compartments in highly migratory and non-migratory melanoma cells. Briefly, PCA analysis was performed on 100Kb binned matrices to assign compartment identity for each bin. For the analysis, interaction zScores, normalizing for interaction decay for genomic distance, were calculated according to the matrix2compartment.pl script in cworld-dekker. Zscore matrices were reordered based on compartment strength (from strongest B to strongest A using eigenvector values). Finally, matrices were smoothed at 500Kb bin size.

Interchromosomal Fraction (ICF)

Ratio of interchromosomal interactions relative to the total number of interactions for a given chromosome as previously described (Heinz et al., 2018).

$$ICF = \frac{Interchromosomal\ Interactions}{Inter + Intra\ chromosomal\ Interactions}$$

deltaICF = ICFBottom - ICFTop

Distal to Local Ratio (DLR)

Log2 ratio of HiC interactions with distance greater than 3Mb relative to local interactions less than 3 Mb away. To find the change in DLR after constricted migration, delta DLR was calculated as $DLR_{Bottom} - DLR_{Top}$ as previously described (Heinz et al., 2018).

$$DLR = log2\frac{Distal\ Interactions\ (> 3Mb)}{Local\ Interactions\ (< 3Mb)}$$

$$deltaDLR = DLRTop - DLRBottom$$

Copy Number Variation Estimation

CNV estimation was performed using the approach available from https://github.com/nservant/cancer-hic-norm (Servant et al., 2018)

Translocation Detection and Frequency Calculation

For the novel translocation visibly evident in 2.5 Mb binned contact maps for Bottom-5 constricted migrated cells, we further pinpointed the specific breaksite on each chromosome (chr5 and chr13) using raw valid pair counts within the region. First, we filtered all valid pair interactions between chr5 and chr13 to include only regions of chr13 between 38.3 and 57.5 Mb (a range of coordinates upstream of the translocation site, which all interact more than expected with chr5). Then, we plotted a histogram of interaction frequencies between each locus along chr5 and this set of chr13 coordinates. We noted a sharp interaction drop within the region

chr5:12.24-12.25 Mb, which represents the translocation breakpoint. We then reversed this process to determine the breakpoint along chr13.

To calculate the percent of chromosomes containing this chr5-13 translocation in each subpopulation, we first found the 2.5 Mb bin with the maximum raw Hi-C counts near the translocation site in Bottom-5 cells. We then calculated an average value for raw Hi-C counts between neighboring bins (one bin off diagonal) in cis on chr7. We then calculated the percent of chromosomes bearing the translocation in any given cell type as the ratio of raw interaction counts at the translocation bin over average interaction counts between neighbors in cis. Given the median triploid karyotype of A375 cells, we then multiplied this % of chromosomes by 3 to estimate a % of cells carrying the translocation.

Distance Decay Scaling Plots

Using 40 and 20 Kb binned iteratively corrected and scaled contact matrices, we extracted contact frequencies between bins at each genomic distance, excluding the diagonal bin (zero distance). A loess fit was then used to find a smooth curve describing interaction decay vs. distance (using the matrix2loess.pl script in cworld-dekker). The interaction frequencies were then normalized to set the maximum value (loess fit interaction value for the minimum distance) for each dataset to 1 and then plotted on a log scale vs. log genomic distance.

RNA-Seq

Library Preparation

For Control, Top-5 and Bottom-5 A375 cells, RNA was extracted, and the library was prepared in out laboratory. Briefly, RNA was extracted using Qiagen RNAeasy plus mini kit (Cat. No. 74134). Cells were lysed and homogenized, spun down in gDNA eliminator columns to remove any genomic DNA. All samples were washed with ethanol and the total RNA was eluted. The quality and quantity of the RNA were quantified using Agilent Bioanalyzer Nano RNA kit. All the libraries used were characterized by a RIN value between 9 and 10. rRNA was depleted using NebNext rRNA Depletion Kit (Cat. No. E6310S). Total RNA was hybridized to the probe followed by RNaseH and DNase I digestion. RNA was then purified using AmpureXP beads from Beckman Coulter (Ref. A63881) at a 2.2x concentration of beads. RNA libraries were prepared using NebNext Ultra II RNA library prep Kit (Cat. No. E7770G). After rRNA depletion, RNA was fragmented (~200 nt) and primed following first and second strand cDNA synthesis. The double stranded cDNA was then purified using AmpureXP beads at a 1.8X concentration. After purification, cDNA libraries were end prepped, ligated adapter and PCR amplified for 7 cycles to enrichment for adaptor ligated DNA using NebNext Multiplex Oligos for illumine (Cat. No. E7335G). cDNA librariers were then purified using AmpureXP beads at a 0.9X concentration and their quality was checked using Agilent Bioanalyzer high sensitivity DNA kit. cDNA samples were then sent to Oklahoma Medical Research Facility (OMRF) for high throughput sequencing.

For the rest of A375 libraries, Top20-5, Bottom20-5, Top-12 and Bottom-12, RNA was extracted using the Qiagen RNAeasy plus mini kit as described above. Total RNA was then sent for library preparation and sequencing at GeneWiz.

RNA-Seq Data Analysis

Quality of reads was checked using Fastqc and adapter sequences were trimmed using BBTools (https://github.com/kbaseapps/BBTools). Additionally, quality trimming of the reads was performed and any reads with a lower than 28 quality score were discarded. Reads were then aligned using STAR alignment (https://github.com/alexdobin/STAR) with an average alignment rate of 89%. The aligned reads were then sorted by genomic position and feature counts was performed using htseq 0.11.1(https://github.com/simon-anders/htseq). Differential expression of genes was determined by using DESeq through Galaxy.

ATAC-Seq library preparation and analysis

ATAC-Seq libraries were prepared as previously described (Buenrostro et al., 2015). Libraries were generated using Ad1_noMX and Ad2.1-2.3 barcoded primers from (Buenrostro et al., 2015) and were amplified for a total of 12-13 cycles. The quality and quantity of the libraries were measured using Agilent Bioanalyzer High Sensitivity DNA kit. Sequencing was performed at Oklahoma Medical Research Facility using HiSeq3000 with 75 bp paired end reads.

ATAC-Seq Data Analysis.

Adapters and reads with a quality score less than 20 were trimmed from the final libraries using Skewer/0.2.2 (https://github.com/relipmoc/skewer). Trimmed reads were aligned to the hg19 genome using bowtie2 with default parameters (https://github.com/BenLangmead/bowtie2). Aligned reads were sorted, indexed and ChrM reads were removed using samtools. Duplicated reads were removed using Picard (https://github.com/broadinstitute/picard/blob/master/src/main/java/picard/sam/markduplicates/MarkDuplicates.java). Finally, peaks were called using MACS2 (https://github.com/taoliu/MACS) with the following parameters: --nomodel --extsize 300 -g hs --keep-dup all.

3D Collagen Matrix

Experiments investigating the morphology and migration of A375 cells were performed in single cell suspension in collagen matrices (A375-Control, A375-Top10. A375-Bottom10 generated from passage of A375 through 5 and 12 µm sized pore transwells) as previously described (Denais et al., 2016). 75,000 cells/condition were added into collagen matrices (Rat Tail, Corning 354236) with a density of 2.32 mg/ml. The pH of the collagen gels was normalized to a neutral pH and gels were incubated at 37^0C for 30 min to gel. After the incubation, media with full supplements was supplied to the collagen gels. Cell were allowed to migrate through the collagen for 5 days before the cells were stained and imaged.

Immunofluorescence for collagen.

Cells embedded on collagen were stained as previously described(Denais et al., 2016). Briefly, collagen matrices were fixed in 4% formaldehyde for 30 min at 37C. Collagen matrices were then washed with 1xPBS for 10 min for three times. Each collagen matrix was then incubated with blocking buffer (0.5% Triton, 10% Goat Serum in 1xPBS) overnight at 4C. After blocking, samples were then incubated with primary antibody (LaminA – sc376248) at a 1:500 dilution in

1xBlocking Buffer:1xPBS at 4C overnight. After incubation, aspirate primary antibody solution and wash three times with 1xPBS for 10 min each. Samples were then incubated in secondary antibody (2 drops/mL of PBS) for 1hr and room temperature. After secondary antibody incubation, samples were then washed with 1xPBS three times for 10 min each. Samples were incubated with DAPI (1µg/mL) for 30 min at RT. Collagen matrices were then washed three times with 1xPBS for 10 min each. Z-stacks of collagen matrices were taken with Leica SP8 confocal microscope at 40x water objective.

3D Organoids

Cell culture

Human foreskin fibroblasts (BJ1) and A375 were trypsinized using standard protocols. Aliquots of 1.2 million cells were washed once with their respective complete culture media (1 ml) by centrifugation (500 rpm, 8 min). Each epithelial (A375) cell pellet was re-suspended in 400 µl of full media and then mixed with the corresponding fibroblast pellet. Cell culture inserts (Millipore. Millicell-CM 12mm) were prepared as suggested by the manufacturer and each chamber was seeded with 400 µl of the cell mixture, along with 600 µl of A375 media in the outside chamber. Organoids were allowed to form for 24 hours prior to imaging and fixation.

Histology

Organoids were fixed by adding 400 and 600 µl of 8% formaldehyde (in PBS pH 7.5) to the insert and outside chambers, respectively, for a final concentration of 4%. Organoids were fixed for 1 hr. at room temperature, followed by three rinses in PBS, and frozen over dry ice in cryomold vessels, using O.T.C. compound (Sakura). Cryo sections were obtained at a nominal thickness of 5 µm and stored at -80ºC.

Organoid sections were stained with Hematoxylin and Eosin (H&E) using the Rapid Chrome Kit (Thermo 9990001), with modifications. After hematoxylin incubation, sections were given a fast acid wash with 0.1% aqueous hydrochloric acid, followed by rinsing in running tap water for 2 min. After eosin staining, sections were cleared with Histoclear (National Diagnostics HS-200) and mounted on histomount (National Diagnostics HS-103).

DATA AND SOFTWARE AVAILABILITY

All relevant data supporting the key findings of this study are available within the article and its Supplementary Information files or from the corresponding author on reasonable request. Hi-C, RNA-Seq, and ATAC-Seq sequence data and processed data for A375 cell line experiments are deposited under GEO:XXXXXXXXX. Software and code used for the analyses presented are available as public github packages, as described in the Methods section.

REFERENCES

ABBAS, A., HE, X., NIU, J., ZHOU, B., ZHU, G., MA, T., SONG, J., GAO, J., ZHANG, M. Q. & ZENG, J. 2019. Integrating Hi-C and FISH data for modeling of the 3D organization of chromosomes. *Nat Commun,* 10**,** 2049.

ANDERS, S., PYL, P. T. & HUBER, W. 2015. HTSeq--a Python framework to work with high-throughput sequencing data. *Bioinformatics,* 31**,** 166-9.

BARUTCU, A. R., LAJOIE, B. R., MCCORD, R. P., TYE, C. E., HONG, D., MESSIER, T. L., BROWNE, G., VAN WIJNEN, A. J., LIAN, J. B., STEIN, J. L., DEKKER, J., IMBALZANO, A. N. & STEIN, G. S. 2015. Chromatin interaction analysis reveals changes in small chromosome and telomere clustering between epithelial and breast cancer cells. *Genome Biol,* 16**,** 214.

BELAGHZAL, H., BORRMAN, T., STEPHENS, A. D., LAFONTAINE, D. L., VENEV, S. V., WENG, Z., MARKO, J. F. & DEKKER, J. 2019. Compartment-dependent chromatin interaction dynamics revealed by liquid chromatin Hi-C. *bioRxiv***,** 704957.

BICKMORE, W. A. & VAN STEENSEL, B. 2013. Genome architecture: domain organization of interphase chromosomes. *Cell,* 152**,** 1270-84.

BRANDAO, H. B., PAUL, P., VAN DEN BERG, A. A., RUDNER, D. Z., WANG, X. & MIRNY, L. A. 2019. RNA polymerases as moving barriers to condensin loop extrusion. *Proc Natl Acad Sci U S A,* 116**,** 20489-20499.

BROERS, J. L., RAYMOND, Y., ROT, M. K., KUIJPERS, H., WAGENAAR, S. S. & RAMAEKERS, F. C. 1993. Nuclear A-type lamins are differentially expressed in human lung cancer subtypes. *Am J Pathol,* 143**,** 211-20.

BUENROSTRO, J. D., WU, B., CHANG, H. Y. & GREENLEAF, W. J. 2015. ATAC-seq: A Method for Assaying Chromatin Accessibility Genome-Wide. *Curr Protoc Mol Biol,* 109**,** 21 29 1-9.

CHAMBERS, A. F., GROOM, A. C. & MACDONALD, I. C. 2002. Dissemination and growth of cancer cells in metastatic sites. *Nat Rev Cancer,* 2**,** 563-72.

DAMSKY, W. E., ROSENBAUM, L. E. & BOSENBERG, M. 2010. Decoding melanoma metastasis. *Cancers,* 3**,** 126-163.

DAVIDSON, P. M., DENAIS, C., BAKSHI, M. C. & LAMMERDING, J. 2014. Nuclear deformability constitutes a rate-limiting step during cell migration in 3-D environments. *Cell Mol Bioeng,* 7**,** 293-306.

DAVIDSON, P. M. & LAMMERDING, J. 2014. Broken nuclei--lamins, nuclear mechanics, and disease. *Trends Cell Biol,* 24**,** 247-56.

DEKKER, J., RIPPE, K., DEKKER, M. & KLECKNER, N. 2002. Capturing chromosome conformation. *Science,* 295**,** 1306-11.

DENAIS, C. M., GILBERT, R. M., ISERMANN, P., MCGREGOR, A. L., TE LINDERT, M., WEIGELIN, B., DAVIDSON, P. M., FRIEDL, P., WOLF, K. & LAMMERDING, J. 2016. Nuclear envelope rupture and repair during cancer cell migration. *Science,* 352**,** 353-8.

DOBIN, A., DAVIS, C. A., SCHLESINGER, F., DRENKOW, J., ZALESKI, C., JHA, S., BATUT, P., CHAISSON, M. & GINGERAS, T. R. 2013. STAR: ultrafast universal RNA-seq aligner. *Bioinformatics,* 29**,** 15-21.

FIDLER, I. J. 2003. The pathogenesis of cancer metastasis: the 'seed and soil' hypothesis revisited. *Nat Rev Cancer,* 3**,** 453-8.

FRIEDL, P., WOLF, K. & LAMMERDING, J. 2011. Nuclear mechanics during cell migration. *Curr Opin Cell Biol,* 23**,** 55-64.

FU, Y., CHIN, L. K., BOUROUINA, T., LIU, A. Q. & VANDONGEN, A. M. 2012. Nuclear deformation during breast cancer cell transmigration. *Lab Chip,* 12**,** 3774-8.

GASPAR-MAIA, A., ALAJEM, A., MESHORER, E. & RAMALHO-SANTOS, M. 2011. Open chromatin in pluripotency and reprogramming. *Nat Rev Mol Cell Biol,* 12**,** 36-47.

GERLITZ, G. & BUSTIN, M. 2010. Efficient cell migration requires global chromatin condensation. *J Cell Sci,* 123**,** 2207-17.

GOLLOSHI, R., SANDERS, J. T. & MCCORD, R. P. 2018. Iteratively improving Hi-C experiments one step at a time. *Methods,* 142**,** 47-58.

GUPTA, G. P. & MASSAGUE, J. 2006. Cancer metastasis: building a framework. *Cell,* 127**,** 679-95.

HARADA, T., SWIFT, J., IRIANTO, J., SHIN, J. W., SPINLER, K. R., ATHIRASALA, A., DIEGMILLER, R., DINGAL, P. C., IVANOVSKA, I. L. & DISCHER, D. E. 2014. Nuclear lamin stiffness is a barrier to 3D migration, but softness can limit survival. *J Cell Biol,* 204**,** 669-82.

HEINZ, S., TEXARI, L., HAYES, M. G. B., URBANOWSKI, M., CHANG, M. W., GIVARKES, N., RIALDI, A., WHITE, K. M., ALBRECHT, R. A., PACHE, L., MARAZZI, I., GARCIA-SASTRE, A., SHAW, M. L. & BENNER, C. 2018. Transcription Elongation Can Affect Genome 3D Structure. *Cell,* 174**,** 1522-1536 e22.

HNISZ, D., WEINTRAUB, A. S., DAY, D. S., VALTON, A. L., BAK, R. O., LI, C. H., GOLDMANN, J., LAJOIE, B. R., FAN, Z. P., SIGOVA, A. A., REDDY, J., BORGES-RIVERA, D., LEE, T. I., JAENISCH, R., PORTEUS, M. H., DEKKER, J. & YOUNG, R. A. 2016. Activation of proto-oncogenes by disruption of chromosome neighborhoods. *Science,* 351**,** 1454-8.

IMAKAEV, M., FUDENBERG, G., MCCORD, R. P., NAUMOVA, N., GOLOBORODKO, A., LAJOIE, B. R., DEKKER, J. & MIRNY, L. A. 2012. Iterative correction of Hi-C data reveals hallmarks of chromosome organization. *Nat Methods,* 9**,** 999-1003.

IRIANTO, J., XIA, Y., PFEIFER, C. R., ATHIRASALA, A., JI, J., ALVEY, C., TEWARI, M., BENNETT, R. R., HARDING, S. M., LIU, A. J., GREENBERG, R. A. & DISCHER, D. E. 2017a. DNA Damage Follows Repair Factor Depletion and Portends Genome Variation in Cancer Cells after Pore Migration. *Curr Biol,* 27**,** 210-223.

IRIANTO, J., XIA, Y., PFEIFER, C. R., GREENBERG, R. A. & DISCHER, D. E. 2017b. As a Nucleus Enters a Small Pore, Chromatin Stretches and Maintains Integrity, Even with DNA Breaks. *Biophys J,* 112**,** 446-449.

JACOBSON, E. C., PERRY, J. K., LONG, D. S., OLINS, A. L., OLINS, D. E., WRIGHT, B. E., VICKERS, M. H. & O'SULLIVAN, J. M. 2018. Migration through a small pore disrupts inactive chromatin organization in neutrophil-like cells. *BMC Biol,* 16**,** 142.

JIN, F., LI, Y., DIXON, J. R., SELVARAJ, S., YE, Z., LEE, A. Y., YEN, C. A., SCHMITT, A. D., ESPINOZA, C. A. & REN, B. 2013. A high-resolution map of the three-dimensional chromatin interactome in human cells. *Nature,* 503**,** 290-4.

KADOTA, K., SUZUKI, K., COLOVOS, C., SIMA, C. S., RUSCH, V. W., TRAVIS, W. D. & ADUSUMILLI, P. S. 2012. A nuclear grading system is a strong predictor of survival in epitheloid diffuse malignant pleural mesothelioma. *Mod Pathol,* 25**,** 260-71.

KIM, H. S., WON, Y. J., SHIM, J. H., KIM, H. J., KIM, J., HONG, H. N. & KIM, B. S. 2019. Morphological characteristics of vasculogenic mimicry and its correlation with EphA2 expression in gastric adenocarcinoma. *Sci Rep,* 9**,** 3414.

KIM, W., BARRON, D. A., SAN MARTIN, R., CHAN, K. S., TRAN, L. L., YANG, F., RESSLER, S. J. & ROWLEY, D. R. 2014. RUNX1 is essential for mesenchymal stem cell proliferation and myofibroblast differentiation. *Proc Natl Acad Sci U S A,* 111**,** 16389-94.

KIND, J., PAGIE, L., DE VRIES, S. S., NAHIDIAZAR, L., DEY, S. S., BIENKO, M., ZHAN, Y., LAJOIE, B., DE GRAAF, C. A., AMENDOLA, M., FUDENBERG, G., IMAKAEV, M., MIRNY, L. A., JALINK, K., DEKKER, J., VAN OUDENAARDEN, A. & VAN STEENSEL, B. 2015. Genome-wide maps of nuclear lamina interactions in single human cells. *Cell,* 163**,** 134-47.

KOZLOWSKI, J. M., HART, I. R., FIDLER, I. J. & HANNA, N. 1984. A human melanoma line heterogeneous with respect to metastatic capacity in athymic nude mice. *J Natl Cancer Inst,* 72**,** 913-7.

KRIJGER, P. H. & DE LAAT, W. 2016. Regulation of disease-associated gene expression in the 3D genome. *Nat Rev Mol Cell Biol,* 17**,** 771-782.

LAMBERT, A. W., PATTABIRAMAN, D. R. & WEINBERG, R. A. 2017. Emerging Biological Principles of Metastasis. *Cell,* 168**,** 670-691.

LAMMERDING, J., FONG, L. G., JI, J. Y., REUE, K., STEWART, C. L., YOUNG, S. G. & LEE, R. T. 2006. Lamins A and C but not lamin B1 regulate nuclear mechanics. *J Biol Chem,* 281**,** 25768-80.

LANGMEAD, B. & SALZBERG, S. L. 2012. Fast gapped-read alignment with Bowtie 2. *Nat Methods,* 9**,** 357-9.

LI, H., HANDSAKER, B., WYSOKER, A., FENNELL, T., RUAN, J., HOMER, N., MARTH, G., ABECASIS, G., DURBIN, R. & GENOME PROJECT DATA PROCESSING, S. 2009. The Sequence Alignment/Map format and SAMtools. *Bioinformatics,* 25**,** 2078-9.

LOVE, M. I., HUBER, W. & ANDERS, S. 2014. Moderated estimation of fold change and dispersion for RNA-seq data with DESeq2. *Genome Biol,* 15**,** 550.

LYONS, S. M., ALIZADEH, E., MANNHEIMER, J., SCHUAMBERG, K., CASTLE, J., SCHRODER, B., TURK, P., THAMM, D. & PRASAD, A. 2016. Changes in cell shape are correlated with metastatic potential in murine and human osteosarcomas. *Biol Open,* 5**,** 289-99.

MACHESKY, L. M. 2008. Lamellipodia and filopodia in metastasis and invasion. *FEBS Lett,* 582**,** 2102-11.

MARCHAL, C., SIMA, J. & GILBERT, D. M. 2019. Control of DNA replication timing in the 3D genome. *Nat Rev Mol Cell Biol*.

MIRNY, L. A., IMAKAEV, M. & ABDENNUR, N. 2019. Two major mechanisms of chromosome organization. *Curr Opin Cell Biol,* 58**,** 142-152.

MIROSHNIKOVA, Y. A., NAVA, M. M. & WICKSTROM, S. A. 2017. Emerging roles of mechanical forces in chromatin regulation. *J Cell Sci,* 130**,** 2243-2250.

NUEBLER, J., FUDENBERG, G., IMAKAEV, M., ABDENNUR, N. & MIRNY, L. A. 2018. Chromatin organization by an interplay of loop extrusion and compartmental segregation. *Proc Natl Acad Sci U S A,* 115**,** E6697-E6706.

OPPENHEIMER, S. B. 2006. Cellular basis of cancer metastasis: A review of fundamentals and new advances. *Acta Histochem,* 108**,** 327-34.

POMBO, A. & DILLON, N. 2015. Three-dimensional genome architecture: players and mechanisms. *Nat Rev Mol Cell Biol,* 16**,** 245-57.

QUINLAN, A. R. & HALL, I. M. 2010. BEDTools: a flexible suite of utilities for comparing genomic features. *Bioinformatics,* 26**,** 841-2.

RAMASWAMY, S., ROSS, K. N., LANDER, E. S. & GOLUB, T. R. 2003. A molecular signature of metastasis in primary solid tumors. *Nat Genet,* 33**,** 49-54.

ROWAT, A. C., JAALOUK, D. E., ZWERGER, M., UNG, W. L., EYDELNANT, I. A., OLINS, D. E., OLINS, A. L., HERRMANN, H., WEITZ, D. A. & LAMMERDING, J. 2013. Nuclear envelope composition determines the ability of neutrophil-type cells to passage through micron-scale constrictions. *J Biol Chem,* 288**,** 8610-8.

ROWLEY, M. J. & CORCES, V. G. 2018. Organizational principles of 3D genome architecture. *Nat Rev Genet,* 19**,** 789-800.

ROWLEY, M. J., NICHOLS, M. H., LYU, X., ANDO-KURI, M., RIVERA, I. S. M., HERMETZ, K., WANG, P., RUAN, Y. & CORCES, V. G. 2017. Evolutionarily Conserved Principles Predict 3D Chromatin Organization. *Mol Cell,* 67**,** 837-852 e7.

SAN MARTIN, R., PATHAK, R., JAIN, A., JUNG, S. Y., HILSENBECK, S. G., PINA-BARBA, M. C., SIKORA, A. G., PIENTA, K. J. & ROWLEY, D. R. 2017. Tenascin-C and Integrin alpha9 Mediate Interactions of Prostate Cancer with the Bone Microenvironment. *Cancer Res,* 77**,** 5977-5988.

SCHWARZER, W., ABDENNUR, N., GOLOBORODKO, A., PEKOWSKA, A., FUDENBERG, G., LOE-MIE, Y., FONSECA, N. A., HUBER, W., HAERING, C. H., MIRNY, L. & SPITZ, F. 2017. Two independent modes of chromatin organization revealed by cohesin removal. *Nature,* 551**,** 51-56.

SERVANT, N., VAROQUAUX, N., HEARD, E., BARILLOT, E. & VERT, J. P. 2018. Effective normalization for copy number variation in Hi-C data. *BMC Bioinformatics,* 19**,** 313.

SPIELMANN, M., LUPIANEZ, D. G. & MUNDLOS, S. 2018. Structural variation in the 3D genome. *Nat Rev Genet,* 19**,** 453-467.

SPILIOPOULOS, K., PESCHOS, D., BATISTATOU, A., NTOUNTAS, I., AGNANTIS, N. & KITSOS, G. 2015. Vasculogenic mimicry: lessons from melanocytic tumors. *In Vivo,* 29**,** 309-17.

STEPHENS, A. D., BANIGAN, E. J., ADAM, S. A., GOLDMAN, R. D. & MARKO, J. F. 2017. Chromatin and lamin A determine two different mechanical response regimes of the cell nucleus. *Mol Biol Cell,* 28**,** 1984-1996.

STEPHENS, A. D., LIU, P. Z., BANIGAN, E. J., ALMASSALHA, L. M., BACKMAN, V., ADAM, S. A., GOLDMAN, R. D. & MARKO, J. F. 2018. Chromatin histone modifications and rigidity affect nuclear morphology independent of lamins. *Mol Biol Cell,* 29**,** 220-233.

STEPHENS, A. D., LIU, P. Z., KANDULA, V., CHEN, H., ALMASSALHA, L. M., HERMAN, C., BACKMAN, V., O'HALLORAN, T., ADAM, S. A., GOLDMAN, R. D., BANIGAN, E. J. & MARKO, J. F. 2019. Physicochemical mechanotransduction alters nuclear shape and mechanics via heterochromatin formation. *Mol Biol Cell,* 30**,** 2320-2330.

STROM, A. R., EMELYANOV, A. V., MIR, M., FYODOROV, D. V., DARZACQ, X. & KARPEN, G. H. 2017. Phase separation drives heterochromatin domain formation. *Nature,* 547**,** 241-245.

TABERLAY, P. C., ACHINGER-KAWECKA, J., LUN, A. T., BUSKE, F. A., SABIR, K., GOULD, C. M., ZOTENKO, E., BERT, S. A., GILES, K. A., BAUER, D. C., SMYTH, G. K., STIRZAKER, C., O'DONOGHUE, S. I. & CLARK, S. J. 2016. Three-dimensional disorganization of the cancer genome occurs coincident with long-range genetic and epigenetic alterations. *Genome Res,* 26**,** 719-31.

TAJIK, A., ZHANG, Y., WEI, F., SUN, J., JIA, Q., ZHOU, W., SINGH, R., KHANNA, N., BELMONT, A. S. & WANG, N. 2016. Transcription upregulation via force-induced direct stretching of chromatin. *Nat Mater,* 15**,** 1287-1296.

TAKEBE, T. & WELLS, J. M. 2019. Organoids by design. *Science,* 364**,** 956-959.

VAN STEENSEL, B. & BELMONT, A. S. 2017. Lamina-Associated Domains: Links with Chromosome Architecture, Heterochromatin, and Gene Repression. *Cell,* 169**,** 780-791.

VENABLES, R. S., MCLEAN, S., LUNY, D., MOTELEB, E., MORLEY, S., QUINLAN, R. A., LANE, E. B. & HUTCHISON, C. J. 2001. Expression of individual lamins in basal cell carcinomas of the skin. *Br J Cancer,* 84**,** 512-9.

WAZIR, U., AHMED, M. H., BRIDGER, J. M., HARVEY, A., JIANG, W. G., SHARMA, A. K. & MOKBEL, K. 2013. The clinicopathological significance of lamin A/C, lamin B1 and lamin B receptor mRNA expression in human breast cancer. *Cell Mol Biol Lett,* 18**,** 595-611.

WILLIS, N. D., COX, T. R., RAHMAN-CASANS, S. F., SMITS, K., PRZYBORSKI, S. A., VAN DEN BRANDT, P., VAN ENGELAND, M., WEIJENBERG, M., WILSON, R. G., DE BRUINE, A. & HUTCHISON, C. J. 2008. Lamin A/C is a risk biomarker in colorectal cancer. *PLoS One,* 3**,** e2988.

WOLF, K., TE LINDERT, M., KRAUSE, M., ALEXANDER, S., TE RIET, J., WILLIS, A. L., HOFFMAN, R. M., FIGDOR, C. G., WEISS, S. J. & FRIEDL, P. 2013. Physical limits of cell migration: control by ECM space and nuclear deformation and tuning by proteolysis and traction force. *J Cell Biol,* 201**,** 1069-84.

XU, H., LYU, X., YI, M., ZHAO, W., SONG, Y. & WU, K. 2018. Organoid technology and applications in cancer research. *J Hematol Oncol,* 11**,** 116.

YANKASKAS, C. L., THOMPSON, K. N., PAUL, C. D., VITOLO, M. I., MISTRIOTIS, P., MAHENDRA, A., BAJPAI, V. K., SHEA, D. J., MANTO, K. M., CHAI, A. C., VARADARAJAN, N., KONTROGIANNI-KONSTANTOPOULOS, A., MARTIN, S. S. & KONSTANTOPOULOS, K. 2019. A microfluidic assay for the quantification of the metastatic propensity of breast cancer specimens. *Nat Biomed Eng,* 3**,** 452-465.

ZHANG, Y., LIU, T., MEYER, C. A., EECKHOUTE, J., JOHNSON, D. S., BERNSTEIN, B. E., NUSBAUM, C., MYERS, R. M., BROWN, M., LI, W. & LIU, X. S. 2008. Model-based analysis of ChIP-Seq (MACS). *Genome Biol,* 9**,** R137.

ZHANG, Y., MCCORD, R. P., HO, Y. J., LAJOIE, B. R., HILDEBRAND, D. G., SIMON, A. C., BECKER, M. S., ALT, F. W. & DEKKER, J. 2012. Spatial organization of the mouse genome and its role in recurrent chromosomal translocations. *Cell,* 148**,** 908-21.

ZHOU, Y., GERRARD, D. L., WANG, J., LI, T., YANG, Y., FRITZ, A. J., RAJENDRAN, M., FU, X., SCHIFF, R., LIN, S., FRIETZE, S. & JIN, V. X. 2019. Temporal dynamic reorganization of 3D chromatin architecture in hormone-induced breast cancer and endocrine resistance. *Nat Commun,* 10**,** 1522.